Faculty of Engineering, computer and Mathematical Sciences

School of Mechanical Engineering

Modelling of Magnetic Fields of Permanent Magnets with Diametrical Magnetization

Van Tai Nguyen

A thesis submitted in fulfilment of the

requirement for the degree of

Master of Philosophy

February 2019

Supervisors: Dr Tien-Fu Lu

Assoc. Prof. Paul Grimshaw

School of Mechanical Engineering

The University of Adelaide, 5005

SA, Australia

Declarations

I certify that this work contains no material which has been accepted for the award of any other degree or diploma in my name, in any university or other tertiary institution and, to the best of my knowledge and belief, contains no material previously published or written by another person, except where due reference has been made in the text. In addition, I certify that no part of this work will, in the future, be used in a submission in my name, for any other degree or diploma in any university or other tertiary institution without the prior approval of the University of Adelaide and where applicable, any partner institution responsible for the joint-award of this degree.

I give permission for the digital version of my thesis to be made available on the web, via the University's digital research repository, the Library Search and also through web search engines, unless permission has been granted by the University to restrict access for a period of time

Author's signature: Date: *14/02/2019*

Acknowledgements

This thesis could not have been completed without the great support and guidance of my supervisors, Dr Tien-Fu Lu and A/Prof. Paul Grimshaw. I would like to express special thanks to them for being so patient and supportive while reading my work. Their broad knowledge and constructive feedback have helped me grasp the best knowledge and skills which have assisted me to complete my Master of Philosophy program. Moreover, I believe that this knowledge and these skills will continue to assist me to develop a successful research career. I am so grateful to Dr Will for critically reading some parts of this work. I could never forget to say thank you to my friend Di Gao for having been so helpful to me from the very start of my course. Great thanks go also to Alison-Jane Hunter, who is always patient when correcting my English.

Publications

This work has been disseminated through the following peer-reviewed publications.

Published and submitted journal articles:

V. T. Nguyen and T.-F. Lu, "Analytical expression of the magnetic field created by a permanent magnet with diametrical magnetization," *Progress In Electromagnetics Research C, Vol. 87, pp. 163-174, 2018.*

V. T. Nguyen, T.-F. Lu, P. Grimshaw and W. Robertson, "A novel approach for human intention recognition based on Hall Effect sensors," *Submitted to Mechatronics (Elsevier).*

Conference paper which has been presented:

V. T. Nguyen, T. -F. Lu and P. Grimshaw, "Human intention recognition based on contact-less sensors to control an elbow and forearm assistive exoskeleton," *Proceedings of the 7th International Conference of Asian Society for Precision Engineering and Nanotechnology (ASPEN 2017)*, ARM-P-06, Seoul, Korea, Nov. 2017.

Abstract

Cylindrical/ring-shaped permanent magnets with diametrical magnetization can be found in many applications, ranging from electrical motors to position sensory systems. In order to calculate the magnetic field generated by a permanent magnet of this kind correctly and with low computational cost, several studies have been reported in the literature providing analytical expressions. However, these analytical expressions are either limited for an infinite cylinder or for computing the magnetic field only on the central axis of a finite cylinder. The others are derived to calculate the magnetic field at any point in three-dimensional (3D) space but only with low accuracy. This thesis presents an exact analytical model of the magnetic field generated by a diametrically magnetized cylindrical/ring-shaped permanent magnet with a limited length, which can be used to calculate the magnetic field of any point in 3D space fast and with very high accuracy. The expressions were analytically derived, based on geometrical analysis without calculating the magnetic scalar potential. Also, there is no approximation in the derivation steps that yields the exact analytical model. Three components of the magnetic field are analytically represented using complete and incomplete elliptical integrals, which are robust and have low computational cost. The accuracy and efficiency of the developed analytical model was validated using Finite Element Analysis and compared against existing models.

Contents

List of Figures

List of Tables

Nomenclature

Throughout this thesis, bold font letters denote vectors (e.g. vector **H**), and standard font letters (H) denote scalar values (e.g. H is the scalar value of vector **H**).

Symbols	Descriptions	Units
$\boldsymbol{B}$	Magnetic flux density	T
$\boldsymbol{D}$	Electric flux density	C/m^2
$\boldsymbol{E}$	Electric field intensity	V/m
$\boldsymbol{H}$	Magnetic field strength	A/m
$\boldsymbol{J}$	Magnetic Polarization	T
$\boldsymbol{M}$	Magnetization	A/m
$\boldsymbol{T}$	Torque	N.m
$\boldsymbol{m}$	Magnetic moment	$A.m^2$
H_c	Coercivity	A/m
I	Current	A
Φ	Flux	Wb
ΔV	Elemental volume	m^3
∇f	Gradient of scalar function f	
$\nabla \cdot \boldsymbol{A}$	Divergence of vector **A**	
$\nabla x\, \boldsymbol{A}$	Curl of vector **A**	
σ	Conductivity	S/m
ρ	Electric charge density	C/m^3
μ	Permeability	H/m
μ_0	Permeability of free space	H/m
μ_r	Relative permeability	
χ_m	Susceptibility	

ε	Permittivity	F/m
ε_0	Permittivity of free space	F/m
c	Velocity of light	m^{-1}

Chapter 1

Introduction

Permanent magnets have been widely utilised in various applications [1 – 10]. Amongst them, diametrically magnetised cylindrical/annular permanent magnets are widely utilised in electrical motors [11-14]. For instance, diametrically magnetised rotors have been used in high speed permanent magnet synchronous machines (PMSMs) [13] (Fig. 1.1) and [14] (Fig. 1.2).
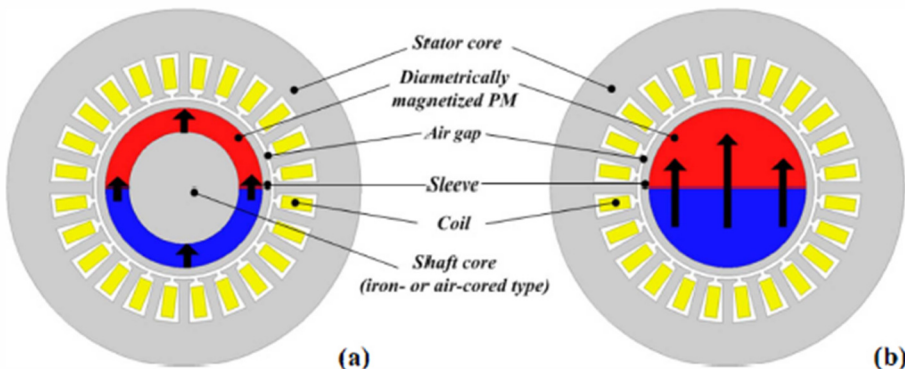
Fig. 1.1 Applications of diametrically magnetised permanent magnets in electrical machines: (a) iron or air cored types; (b) full-ring magnet types [13]
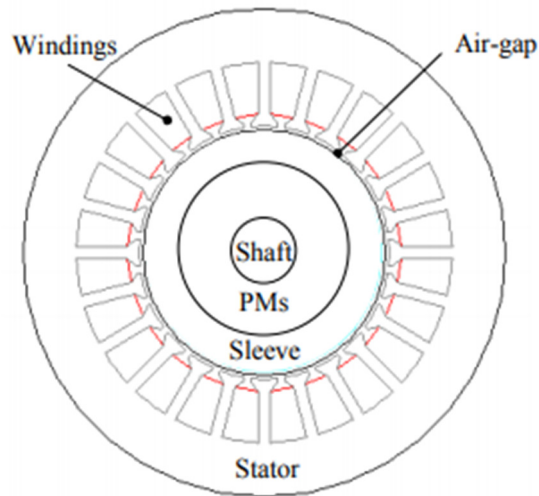
Fig. 1.2 Configuration of 3-phase/24-slots/60000 rpm high speed machine with air-cored diametrically magnetized rotor [14]

These magnets have also been used in non-contact position sensory systems [15-20], mainly due to their ability to produce a sinusoidal air gap magnetic field distribution. For example, a permanent magnet of this kind is used with an array of two Hall effect sensors (Fig. 1.3) [16], whose outputs are sinusoidal, as formulated in Eq. (1.1). These outputs are further processed to obtain a rotation angle of θ [16]. In addition, a diametrically magnetised permanent magnet is used with an array of four Hall effect sensors (Fig. 1.4) [18], as well as with the eccentrically arranged Hall effect sensors (Figs. 1.5, 1.6 and 1.7) [19] for contactless measurement of the rotation angle.
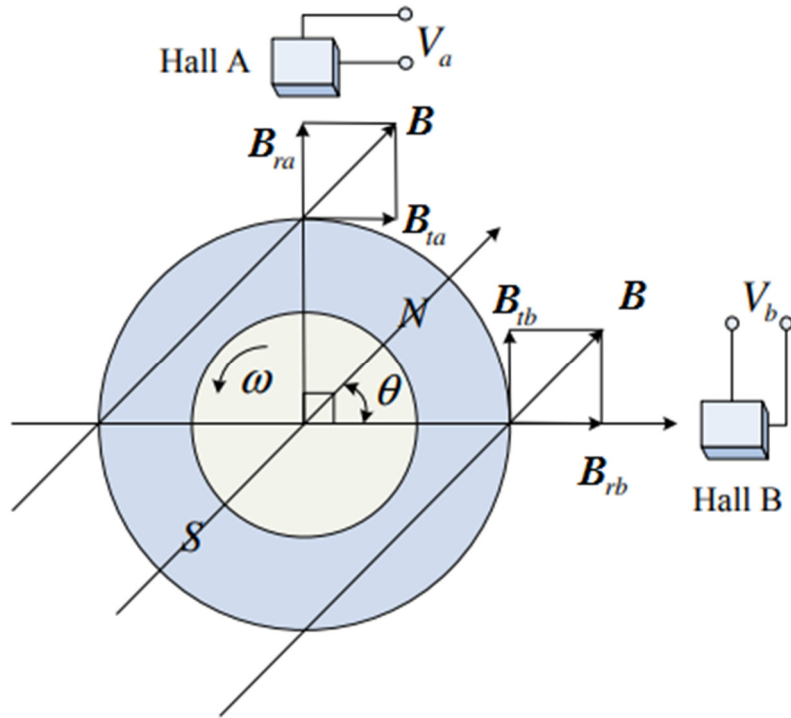
Fig. 1.3 Magnetic field distribution of the magnet ring with diametrical magnetization [16]

The output voltage of Hall A and B in Fig. 1.3 are given respectively, as follows [16]:

$$
\begin{cases}
V_a = R_H \dfrac{I|\mathbf{B}|\sin\theta}{\delta_H} \times 10^{-8} = V\sin\theta \\[2mm]
V_b = R_H \dfrac{I|\mathbf{B}|\cos\theta}{\delta_H} \times 10^{-8} = V\cos\theta
\end{cases}
\tag{1.1}
$$

In this formula (Eq. (1.1)), V is the constant of the sensor. R_H is the Hall material coefficient; I is the exciting current; δ_H is the thickness of the Hall element; **B** is the magnetic flux density.

3

Diametrically magnetised permanent magnet
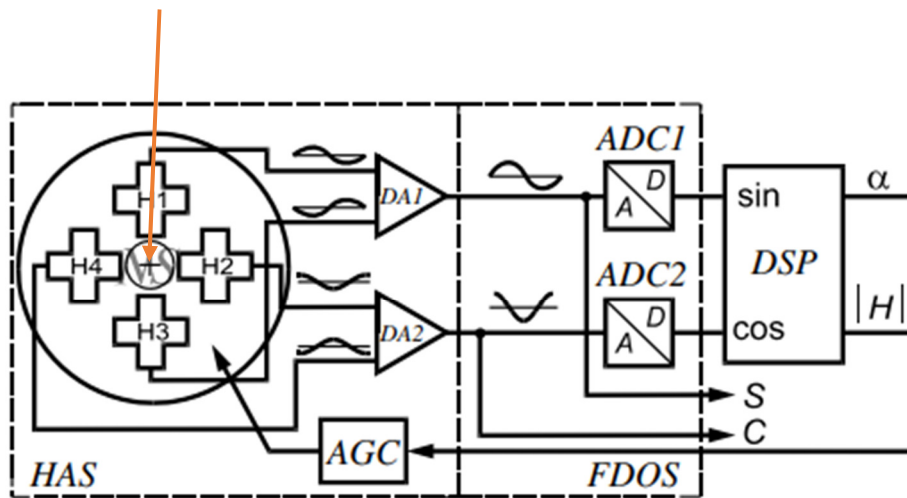
Fig. 1.4 Functional diagram of cyclic displacement converter [18]: HAS – array of Hall effect sensors H1–H4 with differential amplifiers DA1 and DA2; FDOS – former of digital orthogonal components of displacement; ADC1 and ADC2 – analog-to-digital converters; DSP – digital signal processor; AGC – automatic gain control circuit.
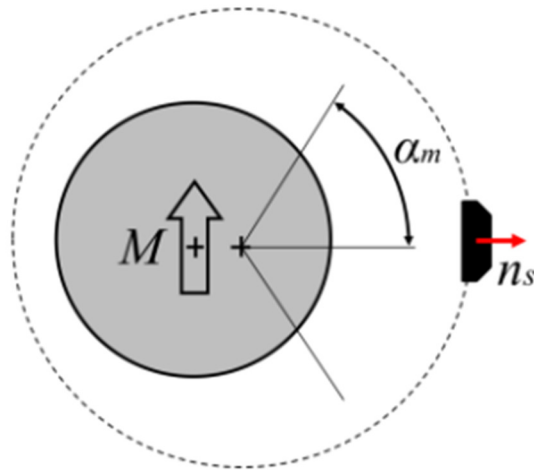
Fig. 1.5 Eccentrically arranged Hall effect sensors and diametrically magnetised permanent magnet [19]: With one sensor
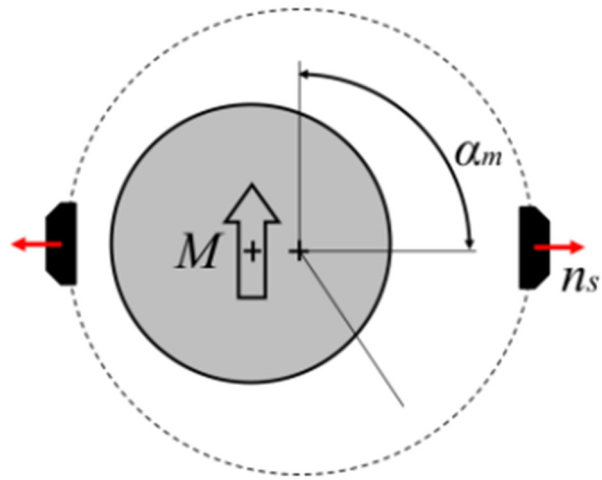
Fig. 1.6 Eccentrically arranged Hall effects sensors and diametrically magnetised permanent magnet [19]: With two sensors
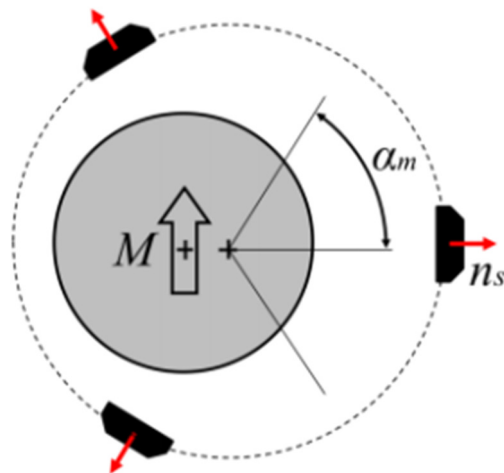
Fig. 1.7 Eccentrically arranged Hall effects sensors and diametrically magnetised permanent magnet [19]: With three sensors

Furthermore, a system of Hall effect senor and annular magnets with diametrical magnetization is also used in the flexion-torsion joint (Fig. 1.8), which is implemented in the Trackhold – A novel passive arm-support device (Fig. 1.9) [20].
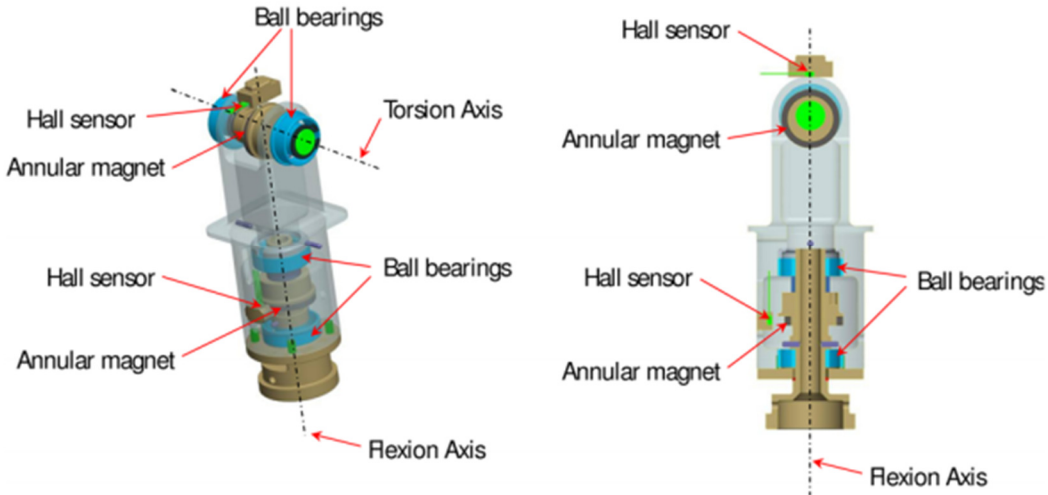
Fig. 1.8 CAD model of a flexion-torsion joint and one of its sections [20]
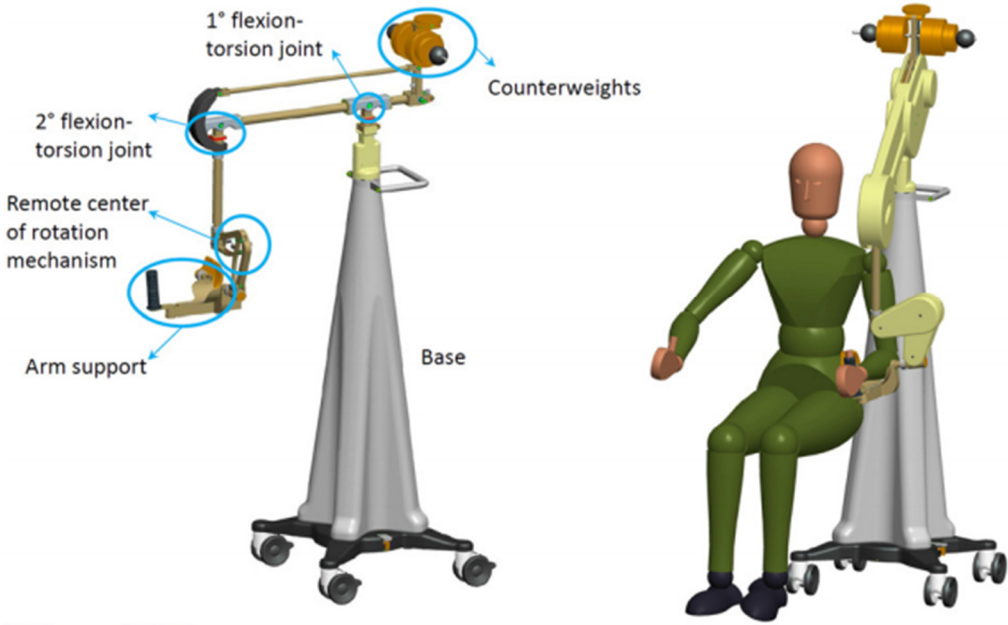
Fig. 1.9 CAD model of the Trackhold [20]

A design for a contactless sensory system, based on Hall effect sensors (Fig. 1.4), which can potentially replace conventionally developed sensory systems based on electromyography (EMG) [21-26], electroencephalography (EEG) [27-33] and force sensors [34-38], to recognise intended motions of the human elbow and forearm, has been proposed by Nguyen et al. [39]. In this system, a ring-shaped magnet, that consists of two semi-ring shaped diametrically magnetised permanent magnet (Fig. 1.10), is implemented and mounted on the user's forearm.

The requirement for an accurate and fast-computed analytical expression of the magnetic field generated by a diametrically magnetised permanent magnet, which can facilitate the parametric design optimization of magnetic devices and model dynamical systems [40 – 41], leads to various ways of expressing the magnetic field of a permanent magnet of this kind. Since it can be time-consuming to use the Finite Element Method, analytical expressions with minimal computational effort have been attracting attention. This is very useful, especially when modelling dynamic systems, such as the movement of magnetic nanoparticles in a magnetic field gradient [42]. Moreover, a fast-computed analytical expression of the magnetic field can help save computational time to solve an optimization problem with variations over a large number of parameters [43].

The aim of this thesis is to develop an accurate and fast-computed analytical model that is simpler and more efficient than those developed in the current literature, to calculate the magnetic field generated by a diametrically magnetised cylindrical/annular permanent magnet at any point of interest in three dimensional space.

7
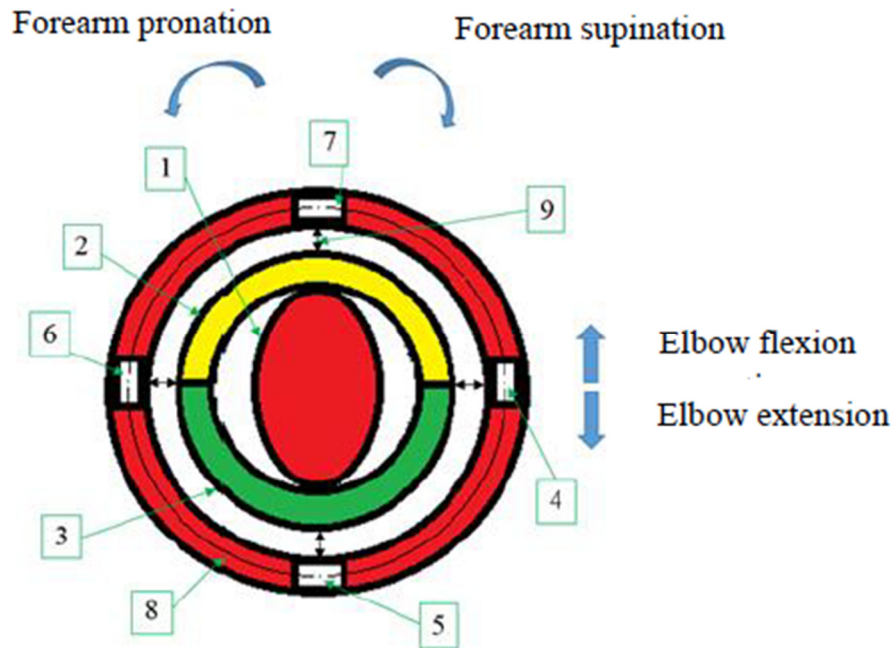
Fig. 1.10 The arrangement of Hall effect sensors and magnets [39]: 1 – Human forearm; 2 - Semi-ring shape diametrically magnetised S-N; 3 - Semi-ring shape diametrically magnetised N-S; 4, 5, 6, and 7 - linear Hall effect sensors; 8 – Exoskeleton sensors' support; 9 – Air gaps.

The exact analytical expressions of the magnetic field, created by a diametrically magnetised cylindrical- and ring- shaped permanent magnet at any point of interest in 3D space, are derived in this thesis based on the Coulombian approach [44], which has been used to analytically model the magnetic fields created by arc-shaped permanent magnets with radial magnetization [45 – 46], ring-shaped permanent magnets with axial and radial magnetization [47, 48], tile permanent magnets with radial magnetization [49] and tangential magnetization [50, 51]. The exact final model of the magnetic field was analytically derived, based on geometrical analysis; and there was no approximation in

8

the derivation steps. All three components of the magnetic field can be expressed using complete and incomplete elliptic integrals that are robust and their computational efforts are minimal [42], [52 − 55]. The accuracy and efficiency of the developed analytical model were validated against currently existing models.

This thesis is organized in six chapters. The current chapter discusses the background of the research topic, the aim of the study, as well as the outline of this thesis. The rest of this thesis is organized as follows:

Chapter 2 presents a review of the current studies for modelling magnetic fields generated by a diametrically magnetised permanent magnet. Chapter 3 provides a theoretical, technical background related to the research topic and the fundamental mathematics used in this thesis. Chapter 4 describes the derivation steps of the analytical expressions of the magnetic field generated by a permanent magnet with diametrical magnetization. Chapter 5 demonstrates the accuracy and efficiency of the derived analytical expressions, compared with the existing models and Finite Element Analysis.

Chapter 6 draws together the conclusions from the project and indicates further studies and applications of the currently developed model.

Chapter 2

Literature review

2.1 Current models to calculate the magnetic field generated by a permanent magnet with diametrical magnetization

The mathematical models existing in the current literature to compute the magnetic field generated by a permanent magnet with diametrical magnetization are reviewed in this chapter.

Even though Finite Element Analysis (FEA) can be a method used to predict the magnetic field correctly, it remains time consuming. Some research has focused on analytical modelling of the magnetic field created by a diametrically magnetised permanent magnet in two dimensional (2D) planes [11-14] to compute the field distribution and provide insights into the magnetic field. However, these 2D models are only suitable for calculating the magnetic field for electrical motors at a point within a boundary condition on the plane under consideration.
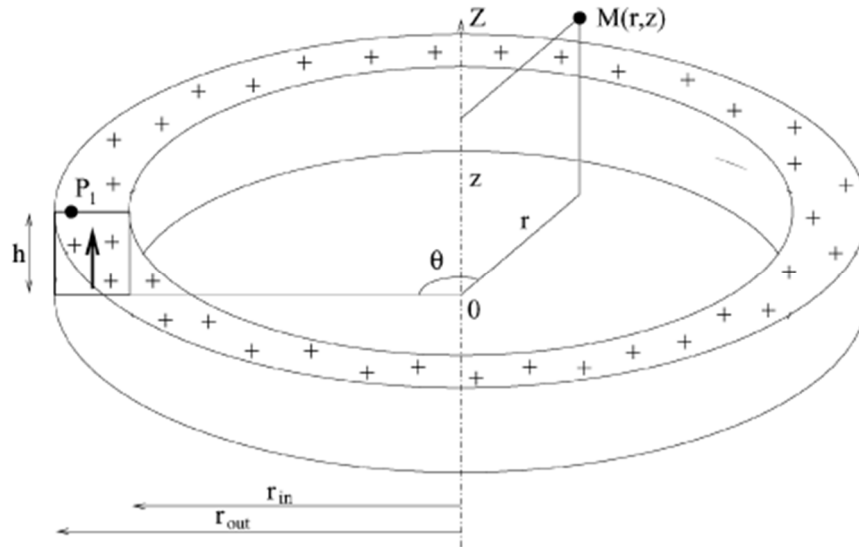
Fig. 2.1 Used geometry of a ring-shaped permanent magnet with axial magnetization: z is an axis of symmetry, its inner radius is r_{in}, its outer radius is r_{out}, its height is h [47]

Currently, based on elliptic integral functions, three dimensional (3D) analytical expressions of a magnetic field created by a ring-shaped permanent magnet [47] with axial (Fig. 2.1) and radial (Fig. 2.2) magnetization and by a radially magnetized tile permanent magnet (Fig. 2.3) [49] have been derived. For these magnets, the surface charge density is constant because the magnetization vectors of these magnets are normal to the corresponding surface of the permanent magnets.
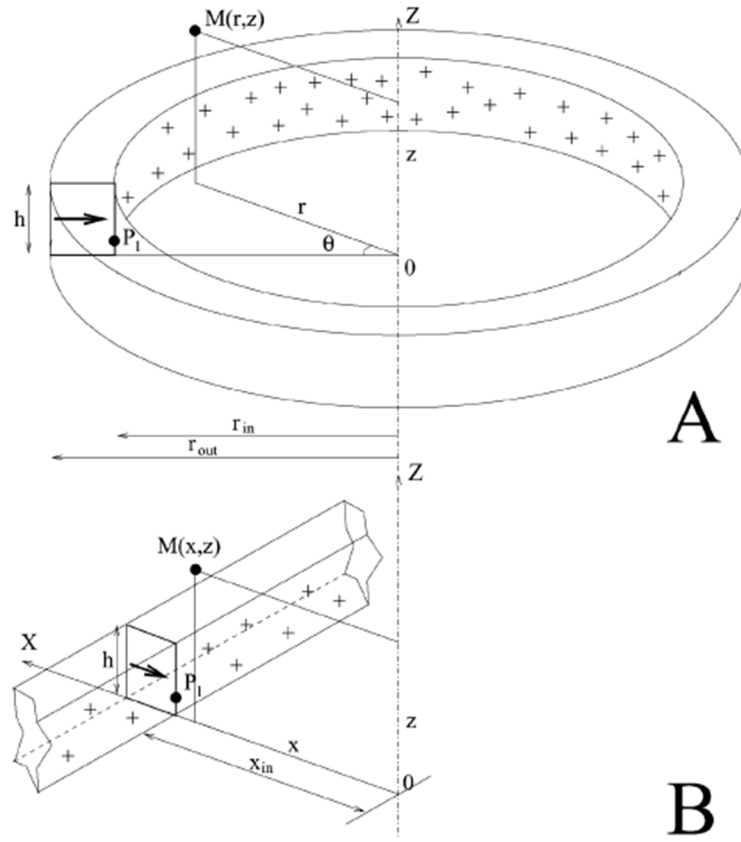
Fig. 2.2 Used geometries; A is a ring whose symmetry axis is z, its inner radius is r_{in}, its outer radius is r_{out}, its height is h, its magnetic polarization is radial: B is an infinitely long parallepiped, its height is h, x_{in} equal r_{in} [47]

However, in the case of a diametrically magnetised permanent magnet, this parameter is dependent on the angle θ (Fig. 2.4) between the magnetization vector **J** and the normal unit vector **n** to the cylindrical surface which is equal to Jcosθ [42]. Therefore, the non-constant surface charge density needs to be taken into account when deriving the analytical expressions of the magnetic field generated by a permanent magnet with
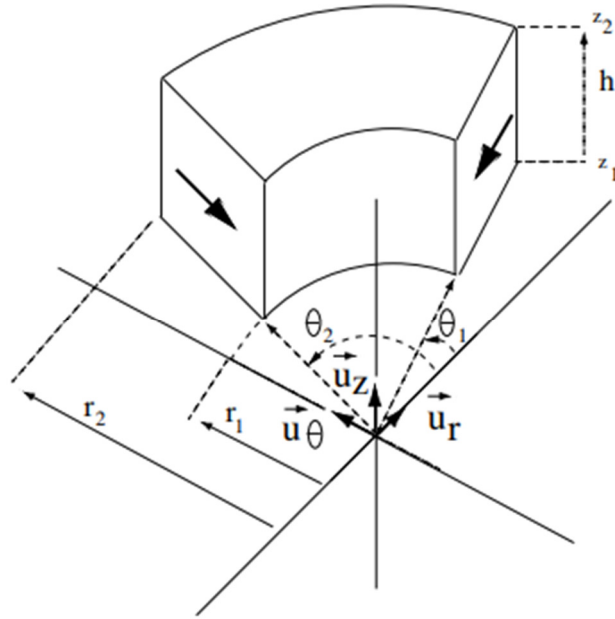
Fig. 2.3 Representation of the geometry of a radially magnetized tile permanent magnet. The tile inner radius is r_1; the tile outer radius is r_2; its height is $h = z_2 - z_1$ and its angular width is $\theta_2 - \theta_1$ [49]

diametrical magnetization. There are some analytical expressions of the magnetic field produced by a diametrically magnetised permanent magnet. However, they are only developed for an infinite cylinder [56 – 57], or for computing the magnetic field on the central axis of a finite cylinder Eq. (2.1) and at the cylinder's centre (z = 0) Eq. (2.2) [58].

$$H_x(z) = \frac{-M_x}{4} \left[\frac{\delta - z}{\sqrt{R^2 + (\delta - z)^2}} + \frac{\delta + z}{\sqrt{R^2 + (\delta + z)^2}} \right] \qquad (2.1)$$

$$H_x(0) = \frac{-M_x}{2} \frac{\delta}{\sqrt{R^2 + \delta^2}} \approx \begin{cases} \frac{-M_x}{2} & \text{for } \delta \gg R \\ \frac{-M_x}{2} \frac{\delta}{R} & \text{for } \delta \ll R \end{cases} \qquad (2.2)$$

In Eqs. (2.1) and (2.2), 2δ is the thickness of the cylindrical magnet, the vector magnetization $\boldsymbol{M}_x$ is along X axis; R is the radius of the cylinder [58].

In order to address these limitations, most recently, Caciagli et al. [42] presented an analytical model, based on complete elliptic integrals, to calculate the magnetic field created by a diametrically magnetised cylindrical permanent magnet with a finite length, at any point in (3D) space. Nonetheless, in the derivation steps, the scalar potential is expressed approximately with the complete elliptic integrals; this caused an error associated with the final expressions of the magnetic field, because these final expressions were derived by taking the derivatives of the approximated scalar potential directly.
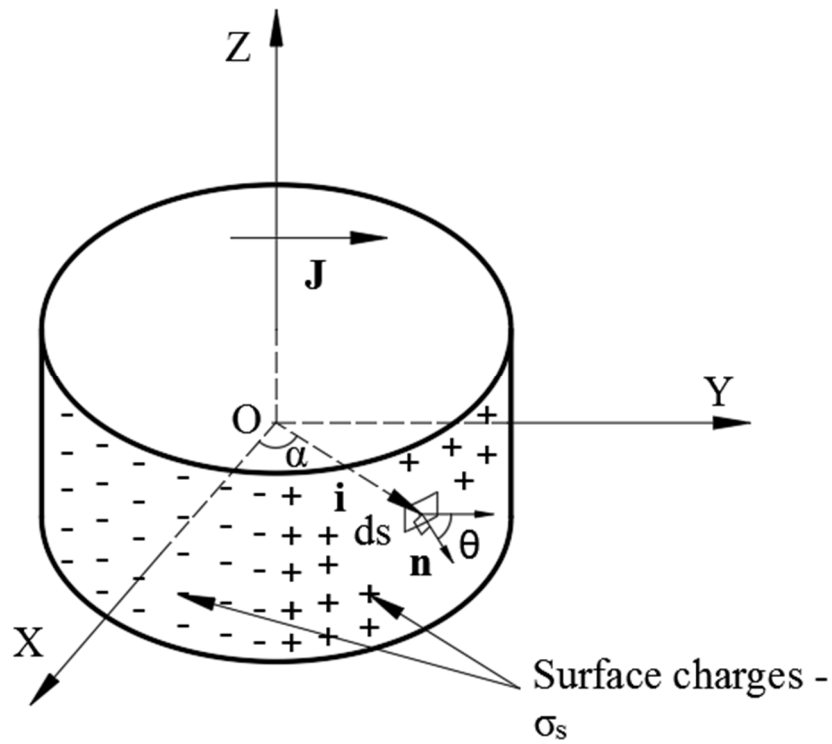
*Fig. 2.4 Cylindrical permanent magnet with diametrical polarization **J** along axis Y*

Other models to calculate the magnetic field were developed and described in the study by Fontana et al. [19]. This study presented the double integration expression (Eq. (2.7), h – thickness of the cylinder), which can be used to calculate the magnetic field created by a permanent magnet with diametrical magnetization at any point of interest in 3D space (Fig. 2.5). However, the double integration expression can only be solved numerically. This can be time-consuming when high accuracy needs to be achieved.
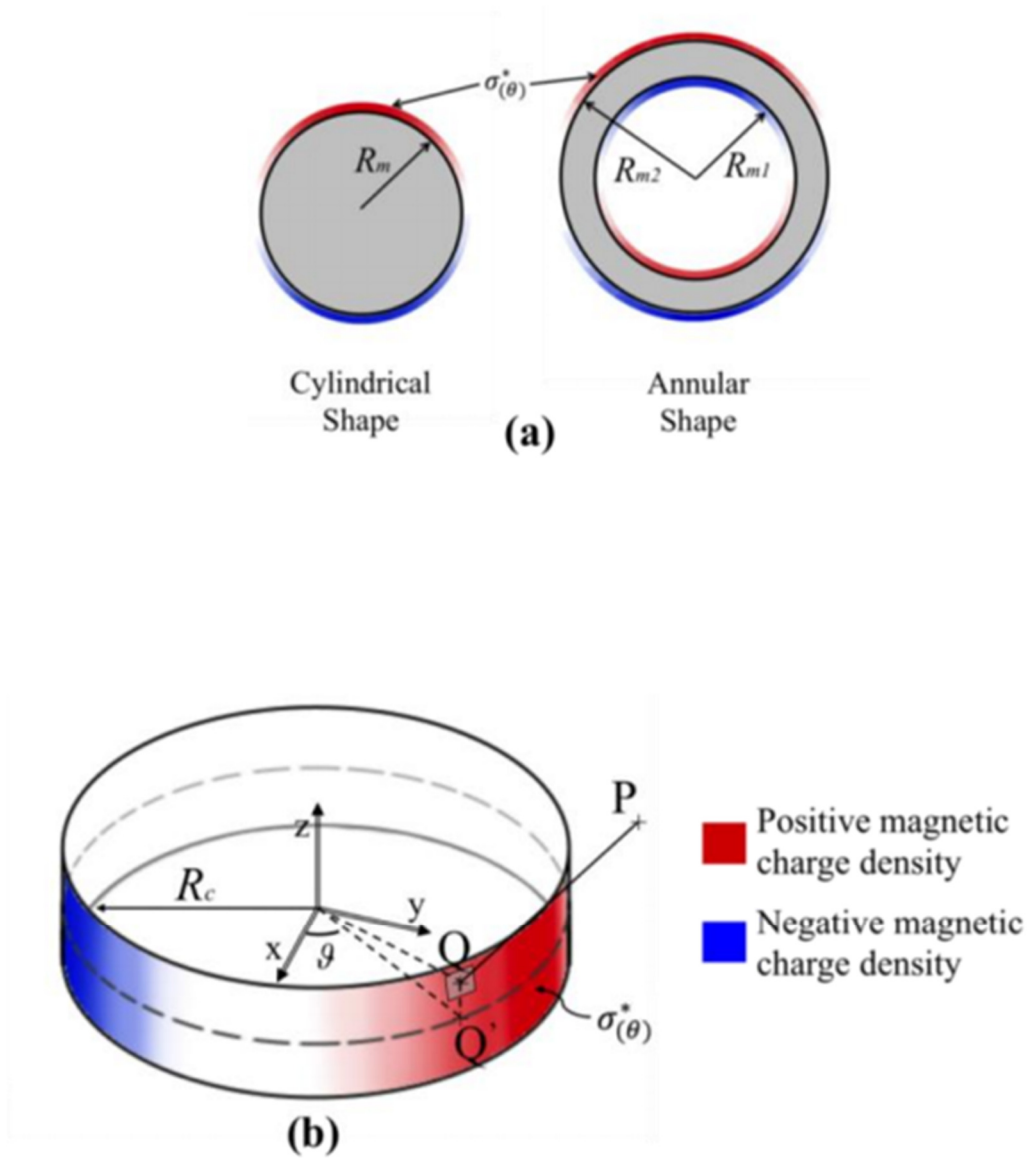
Fig. 2.5 Diametrically magnetised permanent magnets [19]: (a) Scheme of the distribution of the equivalent magnetic charge on the cylindrical surfaces of the cylindrical and annular magnets, (b) Scheme of the geometry and its parameters, σ* - magnetic charge density.

$$\mathbf{H}_{(\rho,\,\varphi,\,z)} = \frac{1}{4\pi\mu_0} \int_{\theta=-\pi}^{\theta=\pi} \int_{z_Q=-\frac{h}{2}}^{z_Q=\frac{h}{2}} \frac{\mathbf{QP}}{|\mathbf{QP}|^3} \sigma_{(\theta)}^* \, R_c \, dz_Q d\theta$$

$$= \frac{M}{4\pi\mu_0} \int_{\theta=-\pi}^{\theta=\pi} \int_{z_Q=-\frac{h}{2}}^{z_Q=\frac{h}{2}} \frac{\mathbf{QP}}{|\mathbf{QP}|^3} \sin(\theta) \, R_c \, dz_Q d\theta \qquad (2.7)$$

The computation of the double integral expression can also be time consuming if the model is used for the optimization process [45]. Recently, single integral expressions (Eq. (2.8)) have been used to calculate the magnetic field at a point on the symmetrical plane of the diametrically magnetised cylindrical permanent magnet and were presented in the study by Fontana et al. [19].

$$H_\rho = \left[\frac{MhR_c}{4\pi\mu_0} \int_{\theta^*=-\pi}^{\theta^*=\pi} \frac{\rho\cos(\theta^*) - R_c\cos^2(\theta^*)}{|\mathbf{Q'P}|^2 \sqrt{\left(\frac{h}{2}\right)^2 + |\mathbf{Q'P}|^2}} d\theta^* \right] \sin(\varphi)$$

$$H_\varphi = \left[\frac{MhR_c}{4\pi\mu_0} \int_{\theta^*=-\pi}^{\theta^*=\pi} \frac{-R_c\sin^2(\theta^*)}{|\mathbf{Q'P}|^2 \sqrt{\left(\frac{h}{2}\right)^2 + |\mathbf{Q'P}|^2}} d\theta^* \right] \cos(\varphi) \qquad (2.8)$$

$$H_z = 0$$

Nevertheless, in this application, the axial component H_z of the field is equal to zero (Eq. (2.8)) and the model can thus only be considered as 2D because its application is limited to the symmetry plane. In other words, the current single integral model cannot be used to compute the magnetic field generated by a cylindrical/ring-shaped permanent magnet with diametrical polarization at any point of interest in the 3D space.

2.2 Gap Statement

Based on the literature review, the knowledge gap can be formulated as follows:

There are no three dimensional (3D) analytical expressions, which are simpler and more efficient than those with double integrals and the current analytical models in the literature, to calculate the magnetic field generated by a diametrically magnetised cylindrical/ring-shaped permanent magnet at any point of interest in the 3D space.

2.3 Aims and Objectives

The general aim of the proposed research is as follows:

The aim of the proposed research is to develop 3D analytical expressions, which are simpler and more efficient than those with double integrals and the current analytical

models in the literature, of the magnetic field generated by a diametrically magnetised cylindrical/ring-shaped permanent magnet at any point of interest in the 3D space.

In order to achieve the aim, the following objectives will be addressed:

Objective 1: To derive the single integral 3D expressions of the magnetic field generated by a diametrically magnetised cylindrical/ring-shaped permanent magnet at any point of interest in 3D space.

Objective 2: To validate the single integral models both analytically and numerically.

Objective 3: To derive the 3D analytical expressions of the magnetic field generated by a diametrically magnetised cylindrical/ring-shaped permanent magnet at any point of interest in 3D space.

Objective 4: To validate the derived analytical model and analyse its efficiency.

Chapter 3

Technical background

This chapter presents fundamental mathematics which is used throughout this thesis. The basic concepts of magnetism and magnetic materials, as well as the Finite Element Analysis and different software used in this thesis are also presented.

The organization of this chapter is summarized in Fig. 3.1.
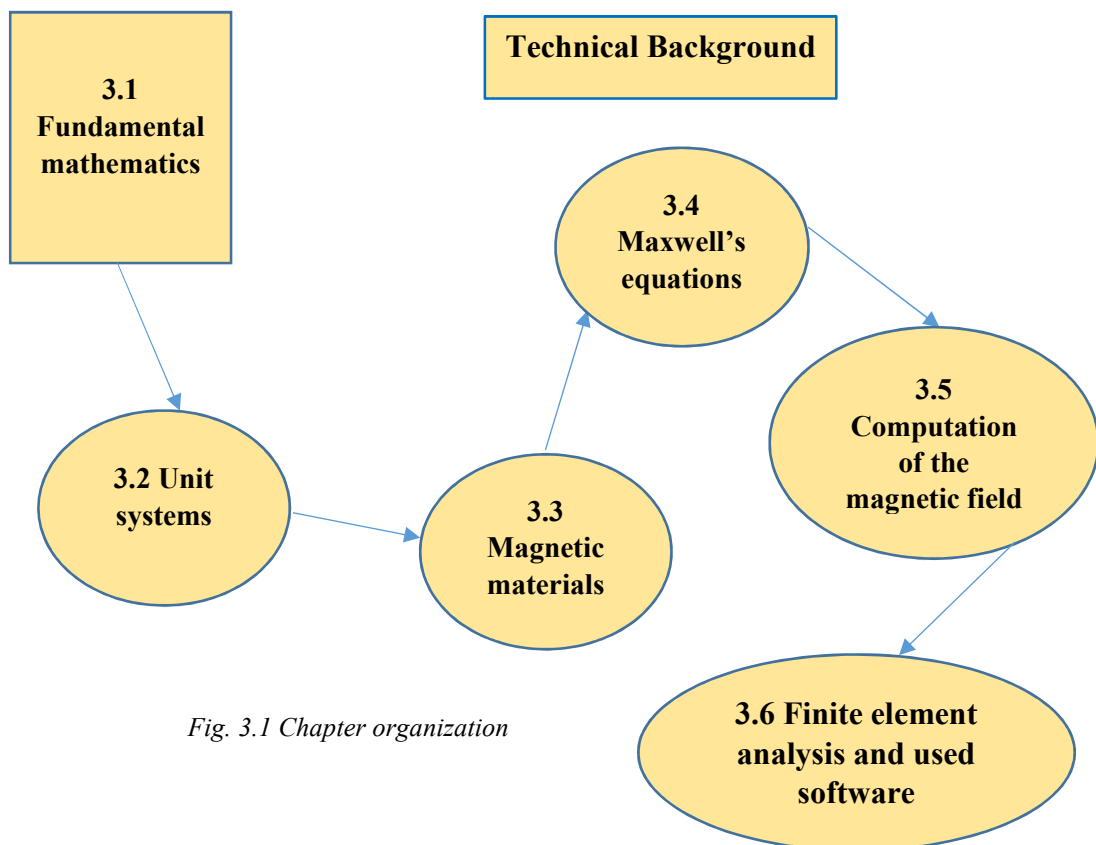
Fig. 3.1 Chapter organization

3.1 Fundamental mathematics

In this section, the Gradient, Divergence and Curl of a vector, which are essential elements for analysis of the magnetic field generated by a permanent magnet, are introduced in both Cartesian and Cylindrical coordinate systems.
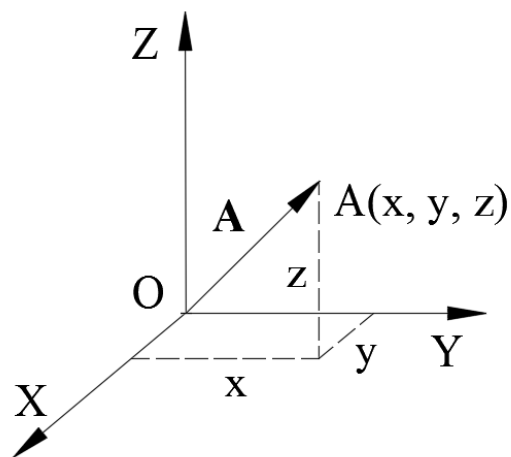
Fig. 3.2 Cartesian coordinate system

3.1.1 The Gradient, Divergence and Curl of a vector in a Cartesian coordinate system

A vector $\mathbf{A}$ with components A_x, A_y, A_z in a Cartesian coordinate system, OXYZ (Fig. 3.2) can be described as follows:

$$\mathbf{A} = A_x\mathbf{x} + A_y\mathbf{y} + A_z\mathbf{z} \qquad (3.1)$$

and magnitudes

$$|\mathbf{A}| = \sqrt{A_x^2 + A_y^2 + A_z^2} \qquad (3.2)$$

Assuming that f(x, y, z) and $\mathbf{A}$(x, y, z) are scalar and vector-valued functions respectively, the vector differential ∇ (del) operator in a Cartesian coordinate system is presented as follows:

$$\text{del} = \nabla = \frac{\partial}{\partial x}\mathbf{x} + \frac{\partial}{\partial y}\mathbf{y} + \frac{\partial}{\partial z}\mathbf{z} \qquad (3.3)$$

and the definitions of the gradient, divergence and curl are follows.

The gradient of scalar function f in a Cartesian coordinate system is:

$$\text{grad } f = \nabla f = \frac{\partial f}{\partial x}\mathbf{x} + \frac{\partial f}{\partial y}\mathbf{y} + \frac{\partial f}{\partial z}\mathbf{z} \qquad (3.4)$$

The gradient of a scalar function plays a vital role in physics and engineering in expressing the relationship between a force field and a potential field (V) (Eq. (3.4.1)) [59]

$$\text{Force } \mathbf{F} = -\nabla \text{ (potential V)} \qquad (3.4.1)$$

The divergence of vector-valued function A in a Cartesian coordinate system is the dot product as follows:

$$\text{div}\mathbf{A} = \nabla \cdot \mathbf{A} = \frac{\partial A_x}{\partial x} + \frac{\partial A_y}{\partial y} + \frac{\partial A_z}{\partial z} \qquad (3.5)$$

The physical meaning of the divergence of vector field **A** at point G can be regarded as the measurement of how much the vector field diverges from the given point.

In the case where **A** flows out of G div**A** > 0 (Fig. 3.3 (a)); **A** flows into G div**A** < 0 (Fig. 3.3 (b)); A flows in and out of G equally div**A** = 0 (Fig. 3.3 (c))

(a)   (b)

(c)
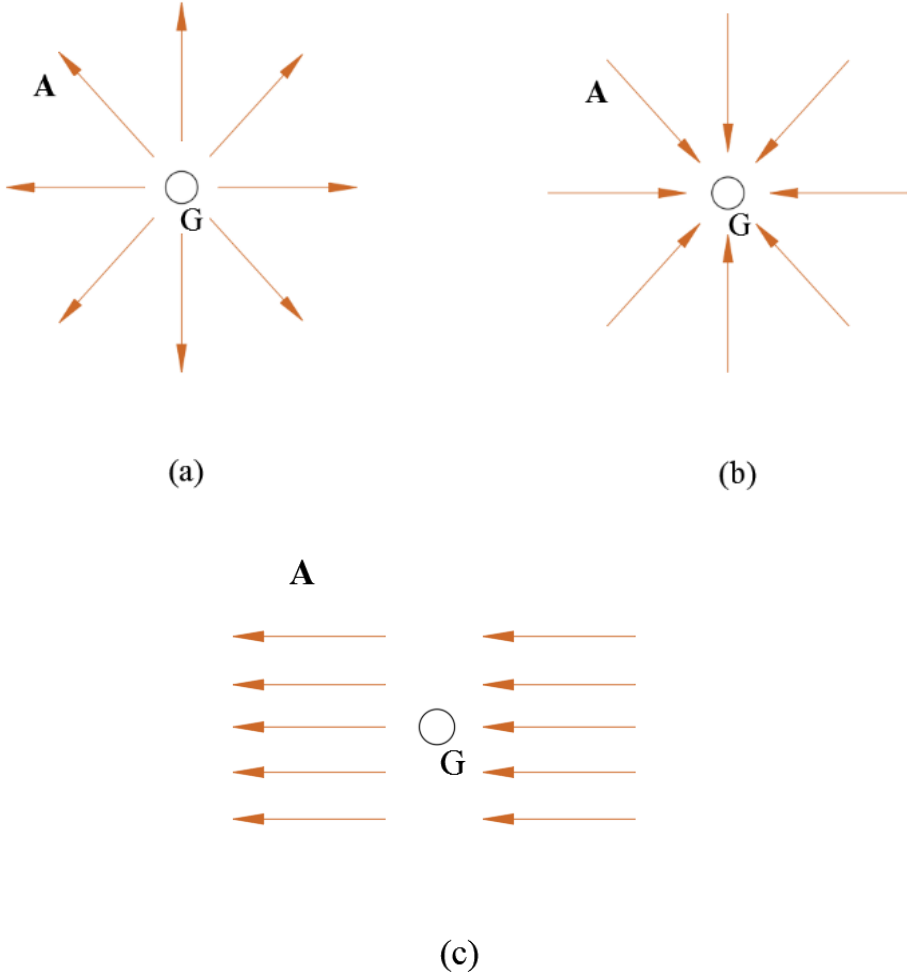
Fig. 3.3 Flow of the vector field A towards point G: (a) A flows out of G, (b) A flows into G, (c) A flows in and out of G

The curl of vector-valued function **A** in a Cartesian coordinate system is the cross product as follows:

$$\text{curl}\mathbf{A} = \nabla \times \mathbf{A} = \begin{vmatrix} \mathbf{x} & \mathbf{y} & \mathbf{z} \\ \dfrac{\partial}{\partial x} & \dfrac{\partial}{\partial y} & \dfrac{\partial}{\partial z} \\ A_x & A_y & A_z \end{vmatrix}$$

$$= \left(\frac{\partial A_z}{\partial y} - \frac{\partial A_y}{\partial z}\right)\mathbf{x} + \left(\frac{\partial A_x}{\partial z} - \frac{\partial A_z}{\partial x}\right)\mathbf{y} + \left(\frac{\partial A_y}{\partial x} - \frac{\partial A_x}{\partial y}\right)\mathbf{z} \qquad (3.6)$$

The physical meaning of Curl of the vector field **A** at point G can be regarded as the measurement of the tendency of the vector **A** to circulate around point G (and the axis of the circulation).
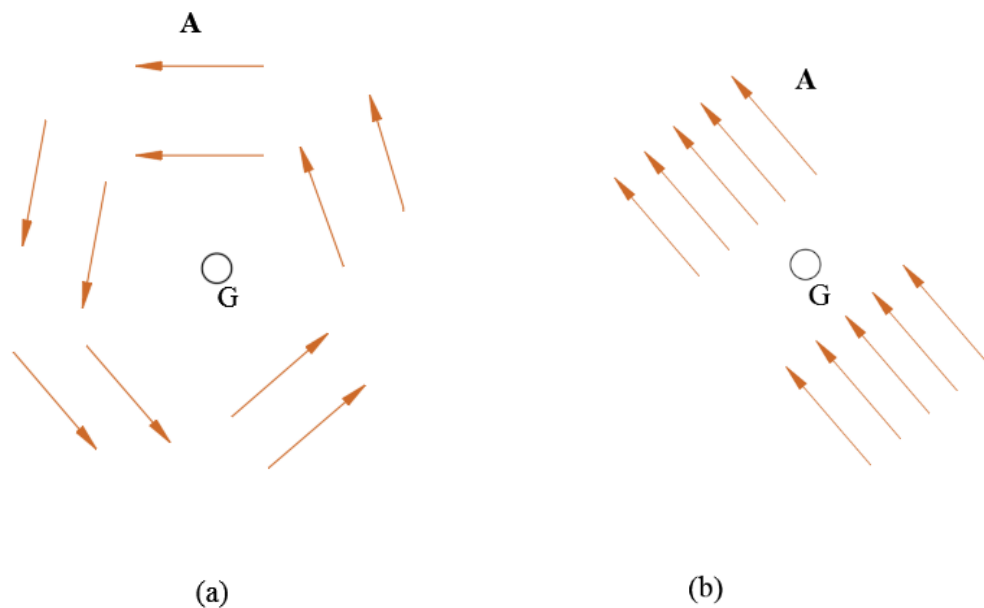
Fig. 3.4 Flow of vector A around point G: (a) vector A tends to swirl around G; (b) vector A has no tendency to swirl around G

24

In the case where vector A tends to swirl around G, curl**A** # 0 (the sign of curl**A** is defined based on the right hand rule; in Fig. 3.4 (a) curl**A** > 0); on the other hand, if there is no tendency for **A** to swirl around G, curl**A** = 0 (Fig. 3.4 (b))

The right hand rule:

Place the right hand at point O (Fig. 3.5). Point the fingers toward the tail of vector **N** and curl the fingers around in the direction of the tip of the vector. If the thumb points toward Z+, the curl of vector **N** possesses positive value and vice versa.
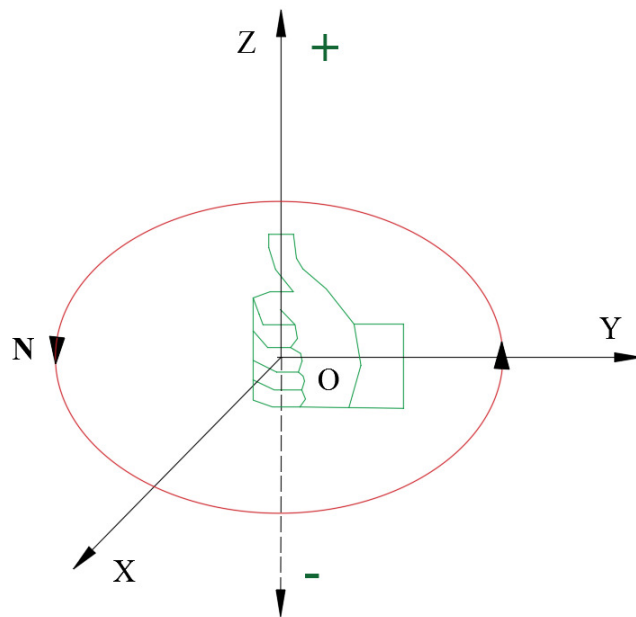
Fig. 3.5 Principle of the right hand rule

3.1.2 Gradient, Divergence and Curl of a vector in a Cylindrical coordinate system

In a cylindrical coordinate system, vector **A** is presented as follows (Fig. 3.6):

$$\mathbf{A} = A_r\mathbf{r} + A_\alpha\boldsymbol{\alpha} + A_z\mathbf{z} \qquad\qquad (3.7)$$

with magnitude

$$A = \sqrt{A_r^2 + A_\alpha^2 + A_z^2} \qquad\qquad (3.8)$$
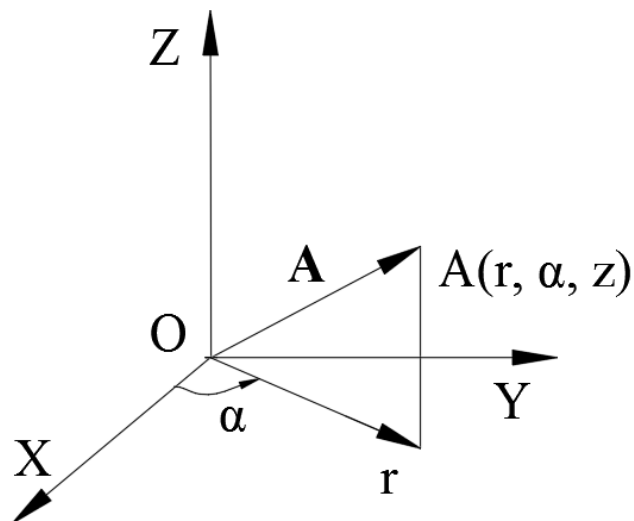
Fig. 3.6 A cylindrical coordinate system

Assuming that f(x, y, z) and **A**(x, y, z) are scalar and vector-valued functions respectively. The vector differential ∇ (del) operator in a cylindrical coordinate system is presented as follows:

$$\nabla = \frac{\partial}{\partial r}\mathbf{r} + \frac{1}{r}\frac{\partial}{\partial \alpha}\boldsymbol{\alpha} + \frac{\partial}{\partial z}\mathbf{z} \qquad (3.9)$$

and the definitions of the gradient, divergence and curl are as follows:

The gradient of the scalar function f in a cylindrical coordinate system is:

$$\nabla f = \frac{\partial f}{\partial r}\mathbf{r} + \frac{1}{r}\frac{\partial f}{\partial \alpha}\boldsymbol{\alpha} + \frac{\partial f}{\partial z}\mathbf{z} \qquad (3.10)$$

The divergence of the vector-valued function **A** in a cylindrical coordinate system is:

$$\nabla \cdot \mathbf{A} = \frac{1}{r}\frac{\partial (rA_r)}{\partial r} + \frac{1}{r}\frac{\partial A_\alpha}{\partial \alpha} + \frac{\partial A_z}{\partial z} \qquad (3.11)$$

and

The curl of the vector-valued function **A** in a cylindrical coordinate system is:

$$\nabla \times \mathbf{A} = \begin{vmatrix} \mathbf{r} & r\boldsymbol{\alpha} & \mathbf{z} \\ \dfrac{\partial}{\partial r} & \dfrac{\partial}{\partial \alpha} & \dfrac{\partial}{\partial z} \\ A_r & rA_\alpha & A_z \end{vmatrix}$$

$$= \left(\frac{1}{r}\frac{\partial A_z}{\partial \alpha} - \frac{\partial A_\alpha}{\partial z}\right)\mathbf{r} + \left(\frac{\partial A_r}{\partial z} - \frac{\partial A_z}{\partial r}\right)\boldsymbol{\alpha} + \frac{1}{r}\left(\frac{\partial (rA_\alpha)}{\partial r}\right.$$

$$\left. - \frac{\partial A_r}{\partial \alpha}\right)\mathbf{z} \qquad (3.12)$$

3.1.3 Summary

The Gradient, Divergence and Curl of scalar f and vector **A** in Cartesian and cylindrical coordinate systems is summarized in Table 3.1 below:

Table 3.1 Gradient, Divergence and Curl of a vector

Operators	Symbols	Cartesian coordinate system	Cylindrical coordinate system
Gradient	∇f	$\dfrac{\partial f}{\partial x}\mathbf{x} + \dfrac{\partial f}{\partial y}\mathbf{y} + \dfrac{\partial f}{\partial z}\mathbf{z}$	$\dfrac{\partial f}{\partial r}\mathbf{r} + \dfrac{1}{r}\dfrac{\partial f}{\partial \alpha}\boldsymbol{\alpha} + \dfrac{\partial f}{\partial z}\mathbf{z}$
Divergence	$\nabla \cdot \mathbf{A}$	$\dfrac{\partial A_x}{\partial x} + \dfrac{\partial A_y}{\partial y} + \dfrac{\partial A_z}{\partial z}$	$\dfrac{1}{r}\dfrac{\partial(rA_r)}{\partial r} + \dfrac{1}{r}\dfrac{\partial A_\alpha}{\partial \alpha} + \dfrac{\partial A_z}{\partial z}$
Curl	$\nabla \times \mathbf{A}$	$\begin{vmatrix} \mathbf{x} & \mathbf{y} & \mathbf{z} \\ \dfrac{\partial}{\partial x} & \dfrac{\partial}{\partial y} & \dfrac{\partial}{\partial z} \\ A_x & A_y & A_z \end{vmatrix}$ $= \left(\dfrac{\partial A_z}{\partial y} - \dfrac{\partial A_y}{\partial z}\right)\mathbf{x} + \left(\dfrac{\partial A_x}{\partial z}\right.$ $\left. - \dfrac{\partial A_z}{\partial x}\right)\mathbf{y} + \left(\dfrac{\partial A_y}{\partial x}\right.$ $\left. - \dfrac{\partial A_x}{\partial y}\right)\mathbf{z}$	$\begin{vmatrix} \mathbf{r} & r\boldsymbol{\alpha} & \mathbf{z} \\ \dfrac{\partial}{\partial r} & \dfrac{\partial}{\partial \alpha} & \dfrac{\partial}{\partial z} \\ A_r & rA_\alpha & A_z \end{vmatrix}$ $= \left(\dfrac{1}{r}\dfrac{\partial A_z}{\partial \alpha}\right.$ $\left. - \dfrac{\partial A_\alpha}{\partial z}\right)\mathbf{r} + \left(\dfrac{\partial A_r}{\partial z}\right.$ $\left. - \dfrac{\partial A_z}{\partial r}\right)\boldsymbol{\alpha} + \dfrac{1}{r}\left(\dfrac{\partial(rA_\alpha)}{\partial r}\right.$ $\left. - \dfrac{\partial A_r}{\partial \alpha}\right)\mathbf{z}$

3.2 Unit systems

The three systems of units [44], which are broadly utilised in magnetism, are the CGS or Gaussian system, MKS and SI systems (International System of Units) referred to as

the Kennelly and Sommerfeld conventions, respectively. As presented in Table 3.2, the flux density **B** is measured in Tesla (T) in SI and in Gauss in CGS; the magnetic field intensity **H** is measured in A/m in SI and in Oe in CGS; the magnetization **M** is measured in A/m in SI and in emu/cm^3 in CGS; the magnetic flux Φ is measured in Webers in SI and in Maxwells in CGS. Table 3.3 presents the conversion factors for these systems.

Table 3.2 Units used in magnetism

Symbol	Description	SI		CGS	
H	Magnetic field strength	A/m	Ampere/ meter	Oe	Oersted
B	Flux density	T	Tesla	G	Gauss
M	Magnetization	A/m	Ampere/ meter	emu/cm^3	Electro-magnetic unit/ centimeter^3
Φ	Flux	Wb	Weber	Mx	Maxwell
σ	Conductivity	S/m	Siemens/ meter	abS/cm	Absiemens/ centimeter
μ_0, μ, μ_r	Permeability	H/m	Henry/meter	emu	Electro-magnetic unit
m	Magnetic moment	A.m^2	Ampere. meter^2	abA.cm^2	Abampere. centimeter^2
I	Current	A	Ampere	abA	abampere
ε	Permittivity	F/m	Farad/meter	esu	Electro-static unit
c	Velocity of light	m^{-1}	Meter^{-1}	cm/s	Centimeter/ second

Table 3.3 Conversion factors

1 Oe = 1000/4π A/m
1 H/m = 10^7/4 π emu
1 Gauss = 10^{-4} T
1 S/m = 10^{-11} abS/cm
1 emu/cm^3 = 1000 A/m
1 Maxwell = 10^{-8} Webers
1 F/m = $4\pi10^{-7}$ c^2 esu

3.3 Magnetic materials

3.3.1 Magnetization, susceptibility and permeability

The fundamental element in magnetism is the magnetic dipole [44]. The magnetic dipole can be considered as a pair of closely spaced magnetic poles (Fig. 3.7) or a small current loop (Fig. 3.8). A magnetic dipole generates a moment **m** (Figs. 3.7 and 3.8) which is measured in A.m^2 in the SI unit system. Let **B** denote the Flux density and **H** denote the Field strength of the magnetic field.
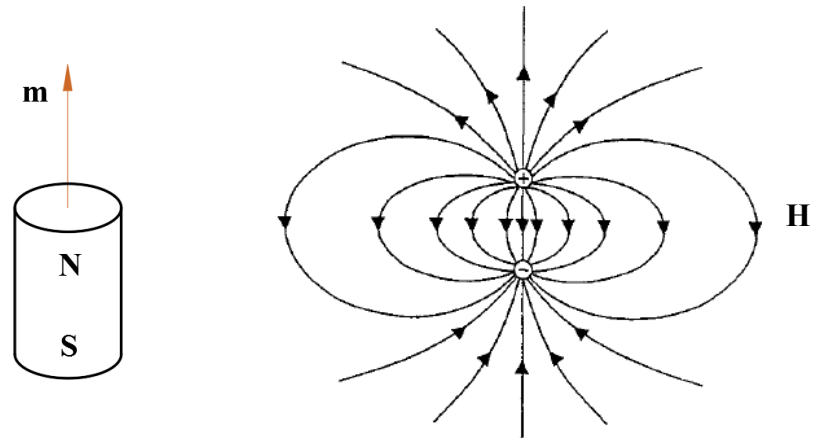
Fig. 3.7 Magnetic dipole: Magnetic charge model and H-field [44]
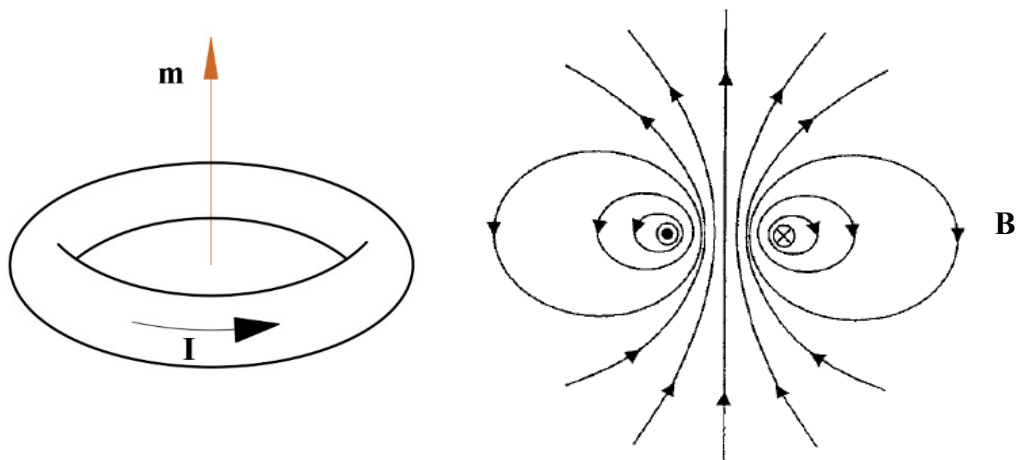
Fig. 3.8 Magnetic dipole: Current loop and B-field [44]

The net magnetic dipole moment per unit volume is defined as magnetization **M**. This parameter can be numerically presented as follows:

$$\mathbf{M} = \lim_{\Delta V \to 0} \frac{\sum_i \mathbf{m}_i}{\Delta V} \qquad (3.13)$$

where $\sum_i \mathbf{m}_i$ is a sum of the dipole moment vectors residing in the elemental volume ΔV.

When an external B-field is applied to a magnetic dipole, it obtains energy as follows:

$$E = -\mathbf{m} \cdot \mathbf{B} \qquad (3.14)$$

and yields a torque $\mathbf{T}$:

$$\mathbf{T} = \mathbf{m} \times \mathbf{B} \qquad (3.15)$$

Eqs. (3.14) and (3.15) can be written in the Kennelly and CGS systems with **H** as follows:

$$E = -\mathbf{m} \cdot \mathbf{H} \qquad (3.16)$$

$$\text{and } \mathbf{T} = \mathbf{m} \times \mathbf{H} \qquad (3.17)$$

The relationship between the magnetic flux density **B** and the magnetic field strength **H** is described in the Sommerfeld convention in the following equation (Eq. 3.18):

$$\mathbf{B} = \mu_0(\mathbf{H} + \mathbf{M}) \qquad (3.18)$$

here, $\mu_0 = 4\pi \times 10^{-7}$ T.m/A is the permeability of free space.

This relationship can be written in the Kennelly convention, as in following equation (Eq. 3.19)

$$\mathbf{B} = \mu_0\mathbf{H} + \mathbf{J} \qquad (3.19)$$

here, **J** is the magnetic polarization whose unit is Tesla. It can be noted that:

$$\mathbf{J} = \mu_0\mathbf{M} \qquad (3.20)$$

In case of linear, homogeneous and isotropic materials, **B** and **M** are proportional to H, as illustrated in Eqs. (3.21) and (3.22):

$$\mathbf{B} = \mu\mathbf{H} \qquad (3.21)$$

and

$$\mathbf{M} = \chi_m\mathbf{H} \qquad (3.22)$$

The constant μ is the permeability and χ_m is the susceptibility of the material. From Eqs. (3.18), (3.21) and (3.22), the relationship between μ and χ_m can be drawn as represented in Eqs. (3.23) or (3.24)

$$\mu = \mu_0(\chi_m + 1) = \mu_0\,\mu_r, \qquad (3.23)$$

or

$$\chi_m = \frac{\mu}{\mu_0} - 1 = \mu_r - 1 \qquad (3.24)$$

where μ_r is the relative permeability of the material.

A material, which has μ depending on **H** (Fig. 3.9), is called nonlinear. For this type of material the relationship between **B**, **M** and **H** can be described as in the following equations:

$$\mathbf{B} = \mu(H)\mathbf{H} \qquad (3.25)$$

and

$$M = \chi_m(H)\mathbf{H} \qquad (3.26)$$
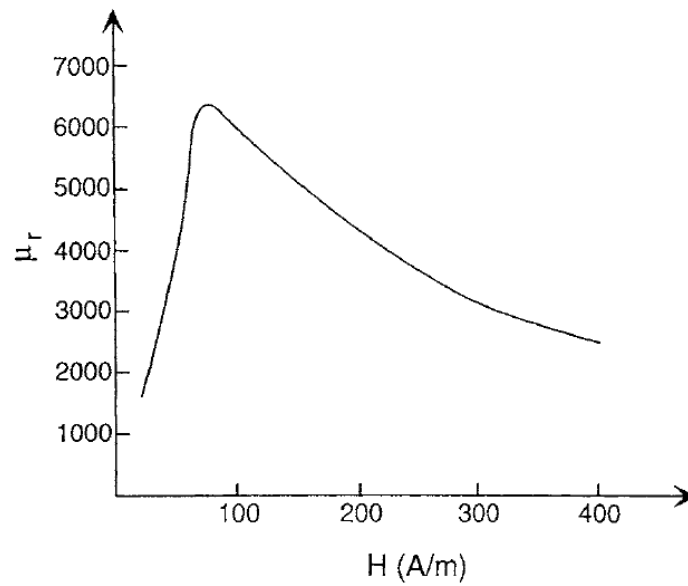
Fig. 3.9 Relative permeability μ_r for silicon steel vs H [44]

3.3.2 Classification of magnetic materials

Based on the magnetic susceptibility (i.e. the behaviours of magnetic dipole moments when magnetic materials are subjected to a magnetic field [60]), magnetic materials can be classified into following five categories [44]:

Diamagnetism: These materials have no net atomic or molecular magnetic moment (to illustrate this phenomenon, there are no arrows, which represent the magnetic moments, in Fig. 3.10). When these materials are subjected to an applied field, atomic currents are

34

generated that give rise to a bulk magnetization that opposes the field. Bismuth (Bi), Mercury (Hg), Silver (Ag) are examples of diamagnetic materials.
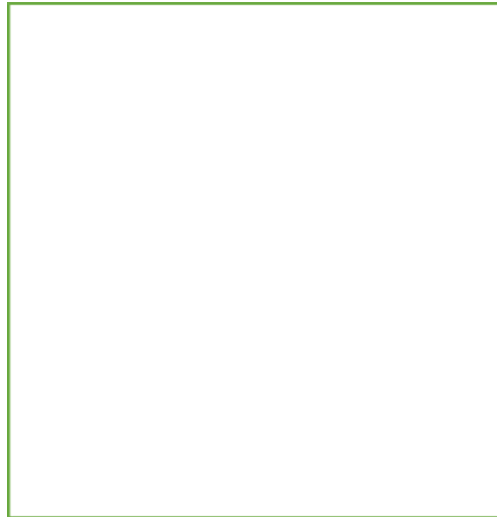
Fig. 3.10 Diamagnetic materials

Paramagnetism: These materials have a net magnetic moment at the atomic level, but the coupling between neighbouring moments is weak (this phenomenon is illustrated in Fig. 3.11; the arrows representing the magnetic moments are randomly aligned as a result of the weak coupling between neighbouring moments). These moments tend to align with an applied field, but the degree of alignment decreases at higher temperatures due to the randomizing effects of thermal agitation. Tungsten (W), Caesium (Cs), Aluminium (Al) are examples of paramagnetic materials.
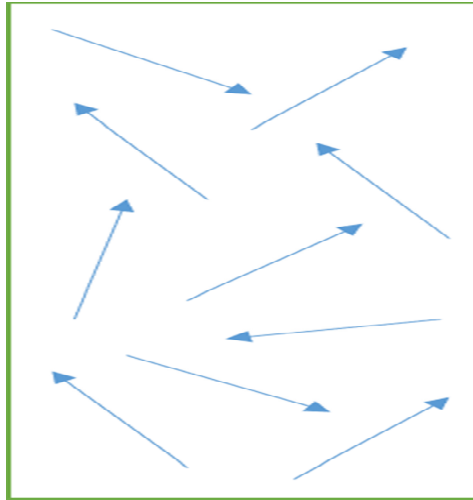
Fig. 3.11 Paramagnetic materials

Ferromagnetism: These materials have a net magnetic moment at the atomic level but, unlike paramagnetic materials, there is a strong coupling between neighbouring moments (this phenomenon is illustrated in Fig. 3.12; the arrows representing the magnetic moments are aligned in the same direction as a result of the strong coupling between neighbouring moments). This coupling gives rise to a spontaneous alignment of the moments over macroscopic regions called domains. The domains undergo further alignment when the material is subjected to an applied field. Cobalt (Co), Iron (Fe), Nickel (Ni) are examples of ferromagnetic materials.
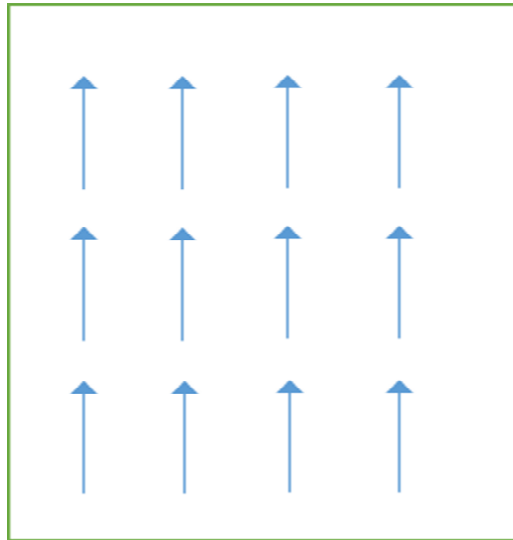
Fig. 3.12 Ferromagnetic materials

Antiferromagnetism and **ferrimagnetism**: These materials have oriented atomic moments with neighbouring moments antiparallel to one another.

In antiferromagnetic materials, the parallel and antiparallel magnetic moments, which are represented by blue and orange colours in Fig. 3.13, are equal. This results in zero net magnetic moment in these materials.

In contrast, the parallel and antiparallel magnetic moments in ferrimagnetic materials, which are represented by blue and orange colours in Fig. 3.14, are unequal. Therefore, there are some net magnetic moment in these materials.
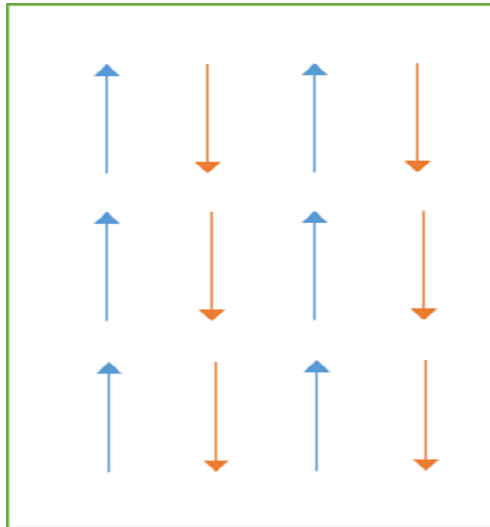
Fig. 3.13 Antiferromagnetic materials
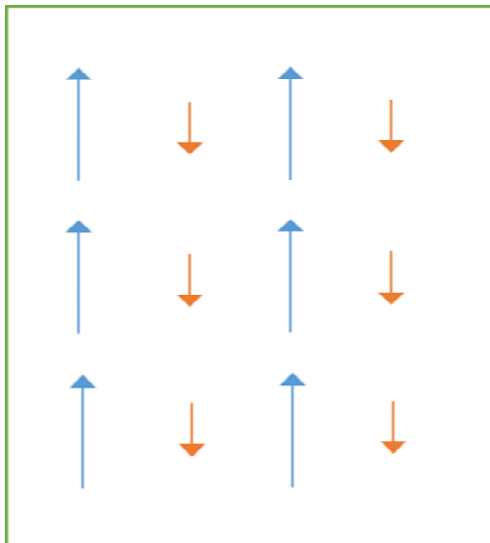
Fig. 3.14 Ferrimagnetic materials

In brief, the classification of magnetic materials can be illustrated in Fig. 3.15, as follows:

All materials

Uncompensated orbital and spin moments present

No magnetic moments

(Vacuum or air, $\mu_r = 1$)

Independent magnetic dipole moments

Exchange coupling in magnetic moments

Diamagnets

No net moment

Aligned opposed to applied field

(Bismuth, $\mu_r = 0.99983$)

Paramagnets

Low net moment

Aligned with applied field

(Aluminium, $\mu_r = 1.0002$)

Ferromagnets

Strong net moment

Aligned with applied field

(Iron, $\mu_r = 5000$)

Ferrimagnets

Net moment

Unequal moments aligned antiparallel

(Nickel ferrite, $\mu_r = 3000$)

Antiferromagnets

No net moment

Moments aligned antiparallel

(Manganese oxide, $\mu_r \approx 1$)

Fig. 3.15 Classification of materials by their alignment of their magnetic dipole moments [60]

Currently ferromagnetic materials are most practically utilised in science and industry [60]. For that reason, this thesis mainly focused in these materials and their basic properties including coercivity, remanence and hysteresis of ferromagnetic materials are outlined in the following sub-sections.

3.3.3 Coercivity and remanence

Coercivity (also called coercive force or the coercive field) for ferromagnetic materials is defined as the strength of the applied magnetic field that is necessary to reduce the magnetisation of the materials to zero. In other words, coercivity determines the resistance of a ferromagnetic material to becoming demagnetized. The unit of coercivity is called an oersted (CGS system) or Ampere/meter (SI system), and it is denoted H_c.

Coercivity can be expressed phenomenologically as follows [61]:

$$H_c = \alpha_k \frac{2K_1}{\mu_0 M_s} - D_{eff} M_s - \Delta H(T, \eta) \qquad (3.27)$$

where K_1 denotes the anisotropy constant, α_k is the Kronmuller parameter, $M_s = |\mathbf{M}|$, D_{eff} is a magnetostatic interaction parameter, and ΔH is the fluctuation-field contribution caused by thermal activation. The term ΔH means that the coercivity depends on the sweep rate $\eta = dH/dt$ [61].

Based on the coercivity, ferromagnetic materials are divided into hard magnetic materials (or permanent magnets) which possess high coercivity, and soft magnetic materials which possess low coercivity. The progress in expanding the range of

coercivity of magnetic materials during the twentieth century is described in Fig. 3.16 [62]; from the softest soft iron to the hardest magnet steel, and now ranges over eight orders of magnitude.
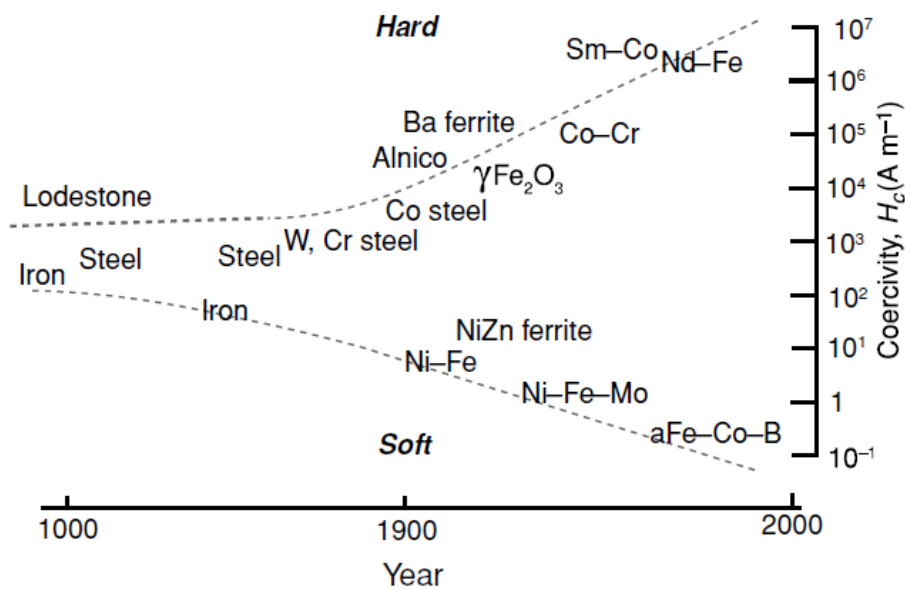
Fig. 3.16 Progress in expanding the range of coercivity of magnetic materials during the twentieth century [62]

 Contrary to the coercivity, the **remanence** (or residual magnetization) is the remaining magnetic induction left behind in a ferromagnetic material after an external field applied to the material is removed. This parameter is represented by the residual flux, which is denoted by **B**$_r$. The properties of some ferromagnetic materials can be found in Table 3.4.

Table 3.4 Properties of some ferromagnetic materials [44]

	SmCo$_5$	Sm$_2$Co$_{17}$	Alnico (cast) 2	Alnico (cast) 5	Ceramic 1	Ceramic 5
B$_r$ (T)	0.83	1.0	0.75	1.24	0.23	0.38
(G)	8300	10000	7500	12400	2300	3800
H$_c$ (kAm^{-1})	600	480	44.6	50.9	147	191
(Oe)	7500	6000	560	640	1850	2400
μ_r	1.05-1.1	1.05	6.4	4.3	1.1	1.1
Density (kg/m^3)	8200	8100	7086	7308	4982	4706
Curie temp. (ºC)	700	750	810	900	450	450

3.3.4 Hysteresis loop

The plot of the magnetic induction **B** or the magnetization **M** as a function of **H,** which can be based on Eq. (3.18) (**B** = μ_0(**H** + **M**)), yields a nonlinear graph called an hysteresis loop (Fig. 3.17). The word *hysteresis* is derived from the Greek word meaning "to lag" [44]. Fig. 3.9 depicts the hysteresis loop which describes the relationship between the magnetization **M** and the magnetic field **H**. In brief, the hysteresis loop presents the irreversible nonlinear response of magnetization **M** to an applied field **H** [62]. In an unmagnetized state, the magnetization **M** is equal to zero. When applied an external field **H**, the magnetization appears, modifies and eventually eliminates the microstructure of ferromagnetic domains magnetized in different directions [62], to reveal the spontaneous magnetization M$_s$. After the applied field is reduced to zero, the

magnetization is not equal to zero but obtains the value of the remanence M_r. In order to decrease the magnetization to zero again, the reverse field, which has the strength of the coercivity H_c, is needed.
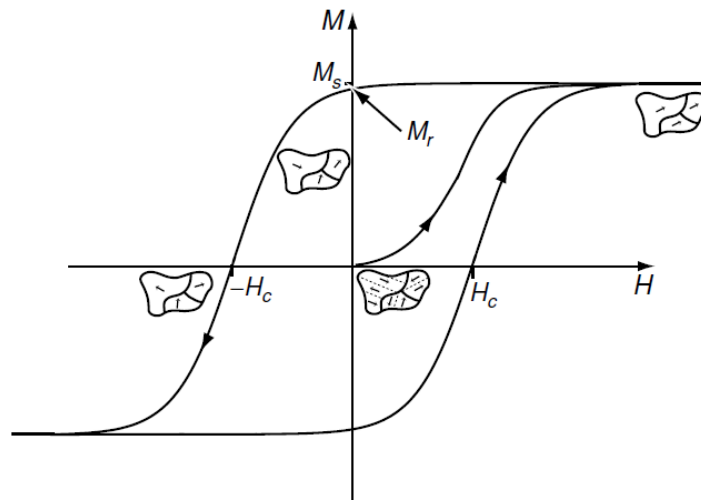
Fig. 3.17 Hysteresis loop of a ferromagnet [62]

For a hard magnetic material which has high coercivity, the hysteresis loop is wide; in contrast, the hysteresis loop of a soft magnetic material is narrow due to its low coercivity (Fig. 3.18).
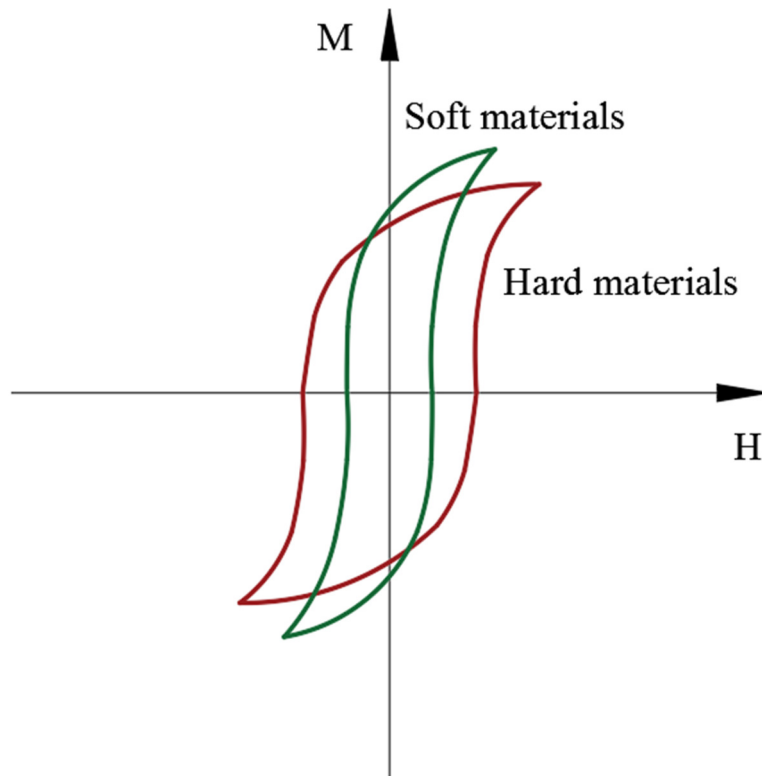
Fig. 3.18 Hysteresis loops for soft and hard magnetic materials [63]

3.4 MAXWELL'S Equations

Maxwell's equations are well-known to be a set of four equations including Gauss's law, Gauss's magnetism law, Faraday's law and Ampere's law, which serve as fundamentals for understanding the behaviour of electromagnetic fields. The equations are presented as follows [44]:

Gauss's law: $$\nabla \cdot \mathbf{D} = \rho \qquad (3.28)$$

Gauss's law for magnetism: $$\nabla \cdot \mathbf{B} = 0 \qquad (3.29)$$

Faraday's law: $$\nabla \times \mathbf{E} = -\frac{\partial \mathbf{B}}{\partial t} \qquad (3.30)$$

Ampere's law: $$\nabla \times \mathbf{H} = \mathbf{J} + \frac{\partial \mathbf{D}}{\partial t} \qquad (3.31)$$

here, $\mathbf{J}$ (A/m^2) and ρ (C/m^3) are the electric current density and the electric charge density, respectively; $\mathbf{E}$ is the electric field intensity (V/m); $\mathbf{D}$ is the electric flux density (C/m^2); $\mathbf{H}$ is the magnetic field intensity (A/m) and $\mathbf{B}$ is the magnetic flux density (T).

In order to provide a complete set of equations for the electric and magnetic fields [44], the constitutive relationships which describe the behaviours of an electromagnetic material are included as follows:

$$\mathbf{B} = \mu_0(\mathbf{H} + \mathbf{M}) \qquad (3.32)$$

$$\mathbf{D} = \varepsilon_0 \mathbf{E} + \mathbf{P} \qquad (3.33)$$

$$\mathbf{J} = \sigma \mathbf{E} \qquad (3.34)$$

here, ε_0 = 8.854 x 10^{-12} F/m is the permittivity of free space; σ (A/V.m) is the conductivity; $\mathbf{P}$ represents the net electric dipole moment per unit volume:

$$\mathbf{P} = \lim_{\Delta V \to 0} \frac{\sum_i \mathbf{P}_i}{\Delta V} \qquad (3.35)$$

where $\sum_i \mathbf{P}_i$ is a sum of the dipole moment vectors residing in the elemental volume ΔV

Under static conditions, the time-dependent terms in Maxwell's equations are ignorable:

$$\frac{\partial \mathbf{D}}{\partial t} = \frac{\partial \mathbf{B}}{\partial t} = 0 \qquad (3.36)$$

Hence, Maxwell's equations reduce to:

$$\nabla \times \mathbf{H} = \mathbf{J} \qquad (3.37)$$

$$\nabla \cdot \mathbf{B} = 0 \qquad (3.38)$$

$$\nabla \times \mathbf{E} = 0 \qquad (3.39)$$

$$\nabla \cdot \mathbf{D} = \rho \qquad (3.40)$$

Eqs. (3.37) and (3.38) are called magnetostatic equations; Eqs. (3.39) and (3.40) are electrostatic equations.

The constitutive relations Eqs. (3.32) – (3.34) in stationary, linear, homogeneous and isotropic media reduce to:

$$\mathbf{B} = \mu\mathbf{H} \qquad (3.41)$$

$$\mathbf{D} = \varepsilon\mathbf{E} \qquad (3.42)$$

where μ and ε are the permeability and permittivity of the media, respectively.

3.5 Computation of the magnetic field

To compute the magnetic field created by a magnetized material, there are three common approaches which can be applied [62]:

(1) The first approach is to integrate over the volume distribution of magnetization *M(r)*;

(2) The second approach is the Amperian approach, which replaces the magnetization by an equivalent distribution of current density j_m;

(3) The third approach is the Coulombian approach, which replaces the magnetization by an equivalent distribution of magnetic charge q_m, which is represented by "-" and "+" signs in Fig. 3.19(c).
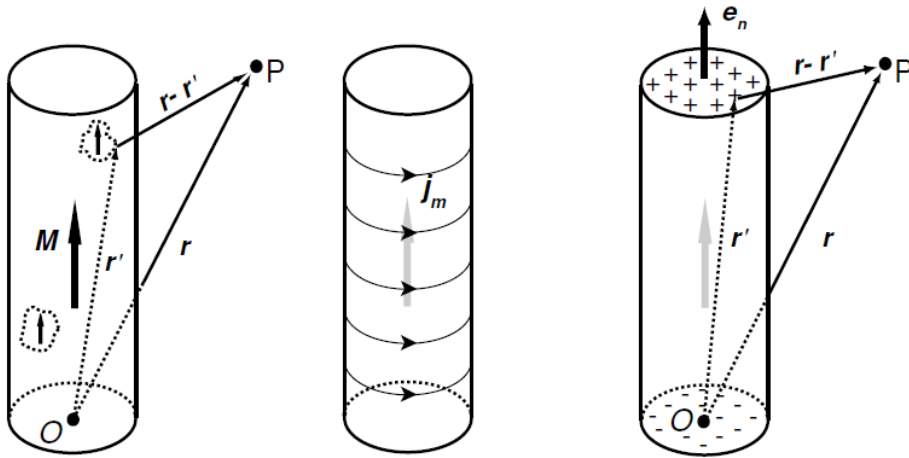
Fig. 3.19 Calculation of the magnetic field outside a uniformly magnetized cylinder by summing: (a) the fields produced by volume distribution of magnetic moments, (b) the fields produced by the distribution of currents, and (c) the fields produced by the distribution of magnetic charge [62]

To illustrate the three approaches, the magnetic field, generated by a cylinder uniformly magnetized along its axis (Fig. 3.19) [62] at point P, can be computed using the following expressions:

(1) The flux density $\mathbf{B}(\mathbf{r})$ is computed by integrating over the volume distribution of magnetization $\mathbf{M}(\mathbf{r})$ (Eq. (3.43)).

$$\mathbf{B}(\mathbf{r})= \frac{\mu_0}{4\pi}\left[\int\left\{\frac{3\mathbf{M}(\mathbf{r}') \cdot (\mathbf{r} - \mathbf{r}')}{|\mathbf{r} - \mathbf{r}'|^5}(\mathbf{r} - \mathbf{r}') - \frac{\mathbf{M}(\mathbf{r}')}{|\mathbf{r} - \mathbf{r}'|^3}\right.\right.$$

$$\left.\left.+ \frac{2}{3}\mu_0\mathbf{M}(\mathbf{r}')\delta(\mathbf{r} - \mathbf{r}')\right\}d^3\mathbf{r}'\right] \qquad (3.43)$$

(2) In the Amperian approach, the equivalent distributions inside and at the surface of the magnetized material are considered (Eq. (3.44)) and the magnetic flux density at point P can be computed using Eq. (3.45) as follows:

$$\mathbf{j}_m = \nabla \times \mathbf{M} \text{ and } \mathbf{j}_{ms} = \mathbf{M} \times \mathbf{e}_n \qquad (3.44)$$

$$\mathbf{B(r)} = \frac{\mu_0}{4\pi}\left\{\int \frac{(\nabla \times \mathbf{M}) \times (\mathbf{r} - \mathbf{r'})}{|\mathbf{r} - \mathbf{r'}|^3} d^3\mathbf{r'} + \int \frac{(\mathbf{M} \times \mathbf{e}_n) \times (\mathbf{r} - \mathbf{r'})}{|\mathbf{r} - \mathbf{r'}|^3} d^2\mathbf{r'}\right\} \qquad (3.45)$$

(3) The Coulombian approach uses the equivalent distributions of the magnetic charge inside (the volume charge) and at the surface (the surface charge) of the magnetized material (Eq. (3.46)). The magnetic field intensity at point P can be computed using Eq. (3.47) as follows:

$$\sigma_v = -\nabla \cdot \mathbf{M} \text{ (volume charge) and } \sigma_s = \mathbf{M} \cdot \mathbf{e}_n \text{ (surface charge)} \qquad (3.46)$$

$$\mathbf{H(r)} = \frac{1}{4\pi}\left\{-\int_V \frac{(\nabla \cdot \mathbf{M}) (\mathbf{r} - \mathbf{r'})}{|\mathbf{r} - \mathbf{r'}|^3} d^3\mathbf{r'} + \int_S \frac{(\mathbf{M} \cdot \mathbf{e}_n) (\mathbf{r} - \mathbf{r'})}{|\mathbf{r} - \mathbf{r'}|^3} d^2\mathbf{r'}\right\} \qquad (3.47)$$

Amongst the three approaches, the Coulombian approach is considered as the easiest method, from a computational perspective, to calculate the magnetic fields generated by

a permanent magnet [62]. This method has also been utilised to produce exact analytical expressions of the magnetic field created by permanent magnets with different magnetizations, as mentioned in the introductory section. Recognising the advantages of this approach, this thesis implements the Coulombian approach to derive the exact analytical model to compute the magnetic field produced by a diametrically magnetised permanent magnet. The details of the implementation are described in Chapter 4.

3.6 Finite element analysis and software used

In the literature, comparing analytical models against the Finite Element model is common practice in this field, even though it does not provide the same level of ground-truth as experimental data can, but a fair comparison can still take place without the need to address possible experimental errors. Therefore, in this study, the calculated results of analytical models were compared with the results of Finite Element Analysis but not with the experimental results.

Finite Element Analysis or the Finite Element Method is a numerical method used to obtain approximate solutions of boundary value problems in engineering and mathematical physics.

The method is characterized by the following features [64]:

1. The problem is divided into smaller domains which are represented by a collection of simple subdomains, called finite elements. This collection of finite elements is called the finite element mesh.

2. Over each finite element, the physical process is approximated by functions of the desired type (polynomials or otherwise), and algebraic equations relating physical quantities at selective points or so-called nodes of the element are developed.

3. The element equations are assembled using the continuity and/or "balance" of the physical quantities.

The cycle of solving a problem using Finite Element Analysis is divided into three major phases:

1. Pre-processing: This phase includes modelling the problem geometry, developing an appropriate finite element mesh, assigning the required materials, (assigning the magnetized direction in the case of electromagnetic analysis) and applying boundary conditions.

2. Solution of the problem: At this step, the governing differential equations are assembled into matrix form and numerically solved.

3. Post-processing: The obtained results are visualized and analysed at this step.

In this thesis, to assist the Finite Element Analysis, electromagnetic simulation software (EMS) from EMWORKS® [65] is utilised. EMS is an effective modelling and simulation software, which has been developed by EMWORKS® to help engineers and academics study numerous problems related to electromagnetic theories and applications; such as calculating the magnetic and electric field and flux, electric potential, voltage, and so forth. The CAD modelling geometries can be done using

SOLIDWORKS®, AUTODESK® or SPACECLAIM, which integrate EMS as a whole to perform the simulation and result analyses easily.

Other software such as MATLAB® and MATHEMATICA® can also be applied to assist in the development and verification of the exact analytical model.

Chapter 4

The derivation of the analytical expressions of the magnetic field generated by a permanent magnet with diametrical magnetization

The derivation steps for the analytical expressions of a magnetic field created by a cylindrical/ring-shaped permanent magnet with diametrical magnetization are divided into two major parts. Firstly, single integral expressions of the magnetic field are derived. Then, the analytical expressions of the magnetic field are derived, based on those single integral expressions.

4.1 Derivation of single integral expressions

A diametrically magnetized cylindrical permanent magnet with parameters is illustrated in Figs. 4.1 and 4.2; its radius is R; its thickness is h; its magnetic polarization $\mathbf{J}$ is assumed to be uniformly diametrical and along axis Y.
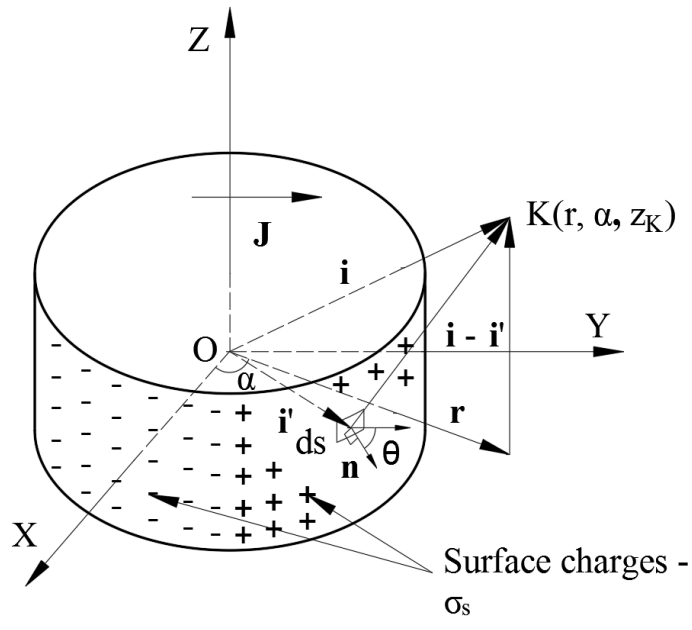
Fig. 4.1 Diametrically magnetized cylindrical permanent magnet: Isometric view
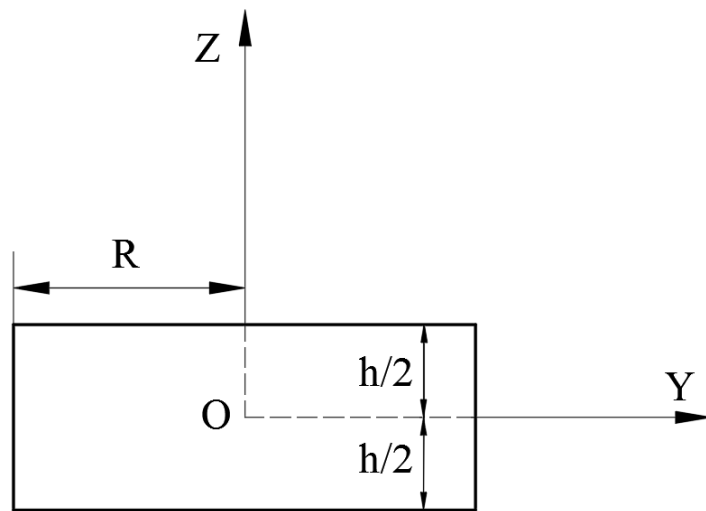
Fig. 4.2 Diametrically magnetized cylindrical permanent magnet: front view
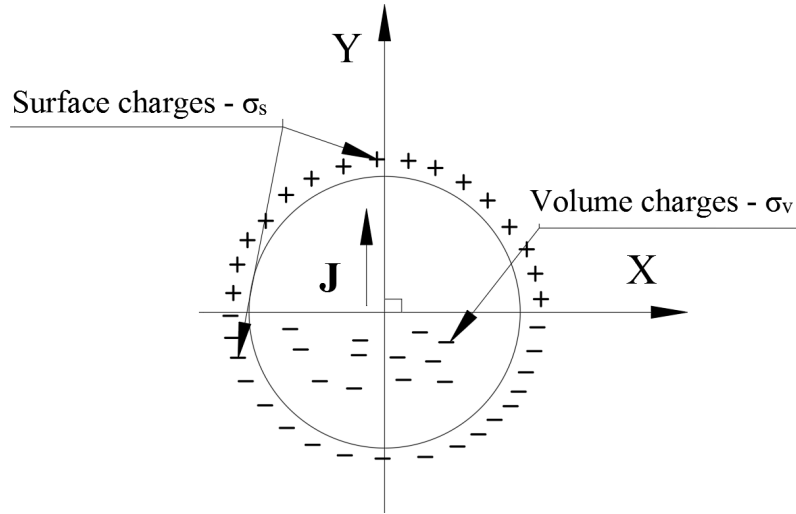
Fig. 4.3 Diametrically magnetized cylindrical permanent magnet: fictitious volume and surface charges from top view

The derivations are based on the Coulombian model in a cylindrical coordinate system (r, α, z) with an azimuth coincident with axis X (Fig. 4.1). According to the Coulombian model, the magnetic field intensity at any observation point K (Fig. 4.1) produced by a permanent magnet in the 3D space can be expressed as follows [45]:

$$\mathbf{H}_K = \frac{1}{4\pi\mu_0}\left(\iint_s \frac{\sigma_s}{|\mathbf{i} - \mathbf{i'}|^3}(\mathbf{i} - \mathbf{i'})ds + \iiint_v \frac{\sigma_v}{|\mathbf{i} - \mathbf{i'}|^3}(\mathbf{i} - \mathbf{i'})dv\right) \qquad (4.1)$$

The volume charge (Fig. 4.3) can be defined as $\sigma_v = -\nabla \cdot \mathbf{J}$, the divergence of the polarization vector $\mathbf{J}$ is equal to zero because it is uniformly diametrical; hence, the magnetic field intensity can be calculated using only the surface charge component, which is the first part of equation in the larger parentheses of Eq. (4.1). The surface charge can be calculated as $\sigma_s = \mathbf{J} . \mathbf{n} = \mathbf{J}\cos\theta = \mathbf{J}\sin(\alpha+\beta)$; here θ is the angle between

55

the polarization vector **J** and the normal unit vector **n** to the cylindrical surface (Fig. 4.1), α is the azimuthal angle and $\beta = \pi/2 - \theta - \alpha$.

After taking the projection of $(\mathbf{i} - \mathbf{i'})$ on the radial, azimuthal and axial directions $(\mathbf{i}_r, \mathbf{i}_\alpha$ and $\mathbf{i}_z$ are the unit vectors respectively), with the consideration that the volume charge makes no contribution to the magnetic field, Eq. (4.1) can be rewritten in the double integration form as follows [19]:

$$\mathbf{H}_K =$$

$$\frac{JR}{4\pi\mu_0} \int_{\beta=-\pi}^{\beta=\pi} \int_{z=-\frac{h}{2}}^{z=\frac{h}{2}} \frac{(r - R\cos\beta)\mathbf{i}_r + (-R\sin\beta)\mathbf{i}_\alpha + (z_K - z)\mathbf{i}_z}{\left(R^2 + r^2 - 2Rr\cos\beta + (z_K - z)^2\right)^{\frac{3}{2}}} \sin(\alpha + \beta) \, dz \, d\beta \qquad (4.2)$$

After analytically integrating (Appendix A) the double integral form of each component of the magnetic field along the axial, azimuthal and radial directions in Eq. (4.2), with the parameterisation shown in Fig. 4.1, the axial, tangential (azimuthal) and radial components of the magnetic field intensity $H_{K(z)}^{(3D)}, H_{K(\alpha)}^{(3D)},$ and $H_{K(r)}^{(3D)}$ along the three directions $\mathbf{i}_z, \mathbf{i}_\alpha,$ and $\mathbf{i}_r$, respectively, can be expressed as detailed in the following sections.

4.1.1 The axial component $H_{K(z)}^{(3D)}(r, α, z)$

The expression of the axial component $H_{K(z)}^{(3D)}(r, α, z)$ was obtained as follows:

$$H_{K(z)}^{(3D)}(r,\ α,\ z) = \left(\frac{JR}{4\pi\mu_0} \int_{β=-π}^{β=π} \left(\frac{1}{\sqrt{\left(\frac{h}{2} - z_K\right)^2 + \left|\overrightarrow{P'K}\right|^2}} \right.\right.$$

$$\left.\left. - \frac{1}{\sqrt{\left(\frac{h}{2} + z_K\right)^2 + \left|\overrightarrow{P'K}\right|^2}} \right) \cos(β)\ dβ \right) \sin(α) \qquad (4.3)$$

where $\left|\overrightarrow{P'K}\right|^2 = R^2 + r^2 - 2Rr\cos(β)$.

4.1.2 The tangential (Azimuthal) component $H_{K(α)}^{(3D)}(r, α, z)$

The expression of the tangential component $H_{K(α)}^{(3D)}(r, α, z)$ was obtained as follows:

$$H_{K(α)}^{(3D)}(r,\ α,\ z) = \left(\frac{JR}{4\pi\mu_0} \int_{β=-π}^{β=π} G\left(\left|\overrightarrow{P'K}\right|^2\right) \left(-R\sin^2(β)\right)\ dβ \right) \cos(α) \qquad (4.4)$$

with,

$$G\left(\left|\overrightarrow{P'K}\right|^2\right) = \frac{\left(\frac{h}{2} - z_K\right)}{\left|\overrightarrow{P'K}\right|^2 \sqrt{\left(\frac{h}{2} - z_K\right)^2 + \left|\overrightarrow{P'K}\right|^2}} + \frac{\left(\frac{h}{2} + z_K\right)}{\left|\overrightarrow{P'K}\right|^2 \sqrt{\left(\frac{h}{2} + z_K\right)^2 + \left|\overrightarrow{P'K}\right|^2}} \qquad (4.4.1)$$

4.1.3 The radial component $H_{K(r)}^{(3D)}(r, \alpha, z)$

The expression of the radial component $H_{K(r)}^{(3D)}(r, \alpha, z)$ was obtained as follows:

$$H_{K(r)}^{(3D)}(r, \alpha, z) = \left(\frac{JR}{4\pi\mu_0} \int_{\beta=-\pi}^{\beta=\pi} G\left(\left| \overrightarrow{P'K} \right|^2 \right) (r\cos(\beta) \right.$$

$$\left. - R\cos^2(\beta)) \, d\beta \right) \sin(\alpha) \qquad (4.5)$$

Here, $G\left(\left| \overrightarrow{P'K} \right|^2 \right)$ is calculated with (4.4.1).

For point K lying on the cylindrical surface (when the radial distance is equal to the radius of the cylinder r = R), Equation (4.5.1) is simplified to

$$H_{K(r)}^{(3D)}(r = R, \alpha, z) =$$

$$\left(\frac{J}{8\pi\mu_0} \int_{\beta=-\pi}^{\beta=\pi} \left(\frac{\left(\frac{h}{2} - z_K \right)}{\sqrt{\left(\frac{h}{2} - z_K \right)^2 + \left| \overrightarrow{P'K} \right|^2}} + \frac{\left(\frac{h}{2} + z_K \right)}{\sqrt{\left(\frac{h}{2} + z_K \right)^2 + \left| \overrightarrow{P'K} \right|^2}} \right) \cos(\beta) \, d\beta \right) \sin(\alpha) \quad (4.5.1)$$

4.2 Verification of the single integral expressions

4.2.1 Analytical verification

In the study by Fontana et al. [19], the single integral expressions of the axial, tangential and radial components of the magnetic field were derived only for point K belonging to the symmetrical plane of the cylinder; that is, for $z_K = 0$. Hence, one of the criteria to

verify the accuracy of the derived single integral expressions is to compare them with those derived by Fontana et al. [19].

4.2.1.1 Analytical verification of the axial component

For point K belonging to the symmetrical plane of the cylinder $z_K = 0$, expression (4.3) can be simplified to $H_{K(z)}^{(Fontana)}(r, \alpha, z_K = 0) = 0$, as presented by Fontana et al. [19].

4.2.1.2 Analytical verification of the tangential component

For point K belonging to the symmetrical plane of the cylinder $z_K = 0$, expression (4.4) can be simplified to

$$H_{K(\alpha)}^{(Fontana)}(r, \alpha, z_K = 0) = \left(\frac{JhR}{4\pi\mu_0} \int_{\beta=-\pi}^{\beta=\pi} \frac{-R\sin^2(\beta)}{\left|\overrightarrow{P'K}\right|^2 \sqrt{\left(\frac{h}{2}\right)^2 + \left|\overrightarrow{P'K}\right|^2}} d\beta \right) \cos(\alpha)$$

as presented by Fontana et al. [19].

4.2.1.3 Analytical verification of the radial component

For point K belonging to the symmetrical plane of the cylinder $z_K = 0$, expression (4.5) can be simplified to

$$H_{K(r)}^{(Fontana)}(r, \alpha, z_K = 0) = \left(\frac{JhR}{4\pi\mu_0} \int_{\beta=-\pi}^{\beta=\pi} \frac{r\cos(\beta) - R\cos^2(\beta)}{|\overrightarrow{P'K}|^2 \sqrt{\left(\frac{h}{2}\right)^2 + |\overrightarrow{P'K}|^2}} d\beta \right) \sin(\alpha)$$

as presented by Fontana et al. [19].

4.2.2 Numerical verification of the single integral expressions

Evaluated in MATLAB R2016b (MATHWORKS), the magnetic field created by diametrically magnetised permanent magnets with different parameters at different points were computed using double integral (Fontana et al. [19]) and the single integral derived in this paper. Table 4.1 shows that the results of the single integral derived in this paper are in very good agreement with those of the double integral presented by Fontana et al. [19].

Table 4.1 Computed magnetic field created by diametrically magnetised permanent magnet with different parameters at different points using the double and single integrals

Magnet parameters (J Tesla, h mm, R mm)	Computed points (r mm, z mm, α°)	Axial component (Tesla) Double integral (Fontana et al. [19]) Single integral derived in this paper	Radial component (Tesla) Double integral (Fontana et al. [19]) Single integral derived in this paper	Tangential component (Tesla) Double integral (Fontana et al. [19]) Single integral derived in this paper
(0.6, 7, 3)	(2, 4, 30°)	4.302514711017279e-02 4.302514691094643e-02	-0.048312471317562 -0.048312471920847	0.012192343565707 0.012192344061685
(0.6, 7, 3)	(1, 4, 45°)	6.313500232306083e-02 6.313500234337720e-02	0.359334310992969 0.359334310748609	0.372800862928376 0.372800862943067
(3, 10, 8)	(3, 5, 60°)	6.306407742139330e+01 6.306407655730165e+01	1.150489775197868 1.150489773290190	1.988313138676867 1.988313138889635
(4, 6, 15)	(6, 7, 90°)	3.523554555045794e+01 3.523554555532005e+01	2.288816392687009e-16 2.281035013194687e-16	3.852052523096182 3.852052523165251
(11, 5, 12)	(9, 12, 38°)	1.147492435815113e+01 1.147492438278891e+01	-0.104000288626235 -0.104000288708199	-0.008341933576704 -0.008341933587258
(5, 6, 8)	(9, -2.5, 30°)	-0.058344205216474 -0.058344205063139	-0.128877649496994 -0.128877649248214	0.134143797427450 0.134143798415742

The developed expressions were implemented in MATLAB R2016b to calculate the three components of the magnetic flux density, both in the air space and inside the magnet, generated by a diametrically magnetised rare earth permanent magnet cylinder (Fig. 4.1 and 4.2) with radius R = 2.5 mm and thickness h = 5 mm; and magnetic remanence J = 0.87 T. In order to verify the results of the analytical models, Finite Element Analysis was built into the Electromagnetic simulation software (EMS) from EMWORKS and integrated with 3D CAD INVENTOR (AUTODESK). The boundary

condition was set to the Normal Flux boundary condition, and the magnet and its close surrounding air region were assigned fine mesh to obtain precise results (Fig. 4.4).
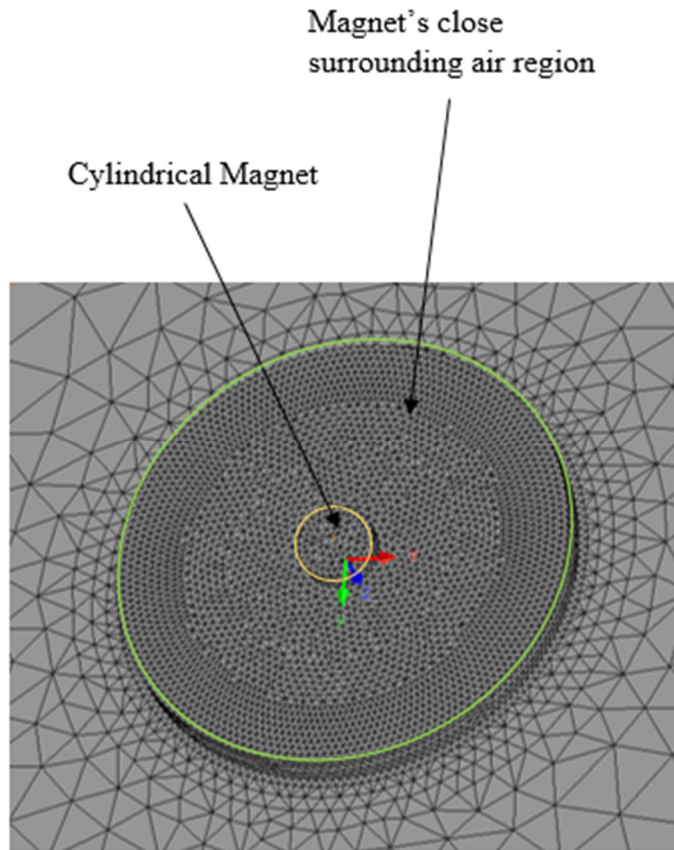
Fig. 4.4 Mesh used for the finite element analysis

Figs. 4.5, 4.6 and 4.7 show that the three components of the magnetic flux density calculated using the developed analytical models are in good agreement with those computed using FEA. The red vertical lines in Figs. 4.5 and 4.6 show a discontinuity of the tangential and radial field components when the radial distance r is equal to the cylinder radius R, due to the discontinuity of the solution that occurs on the surface of the cylinder (Rakotoarison et al. [45]) (the radial component in this case can be

computed using Eq. (4.5.1), and Eq. (4.4) can be used to compute the tangential component). It should be noted that there is an FEA marker point lying on the top end of the line around 2.5 in Fig. 4.7, but there is no marker point lying on the bottom end of the line in the same region. This is due to the inaccuracy of the FEA, as it is time-consuming to set the mesh fine enough to calculate the field component at the exact point r = R. Also, as a result, the analysis confirms that the volume charge in the Coulombian model makes no contribution to the magnetic field generated by a diametrically magnetised cylindrical/annular permanent magnet.
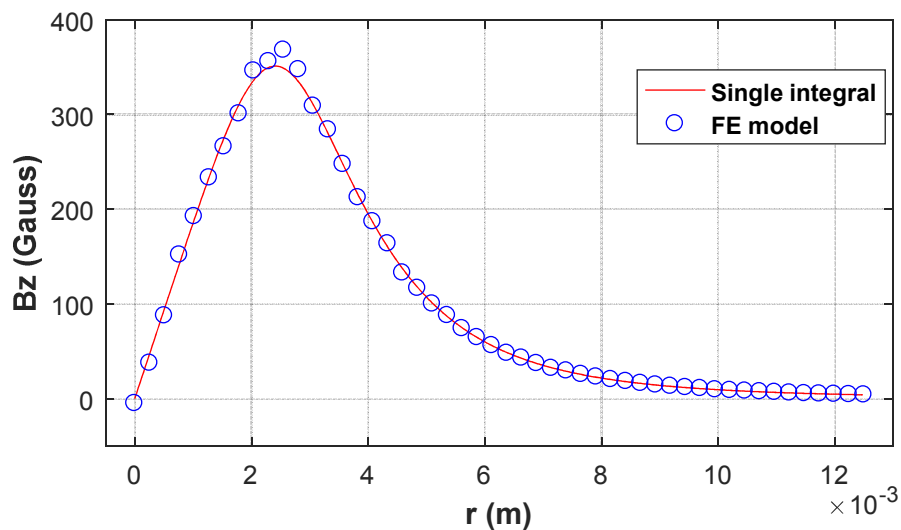
Fig. 4.5 Single integral vs FE model: Axial component
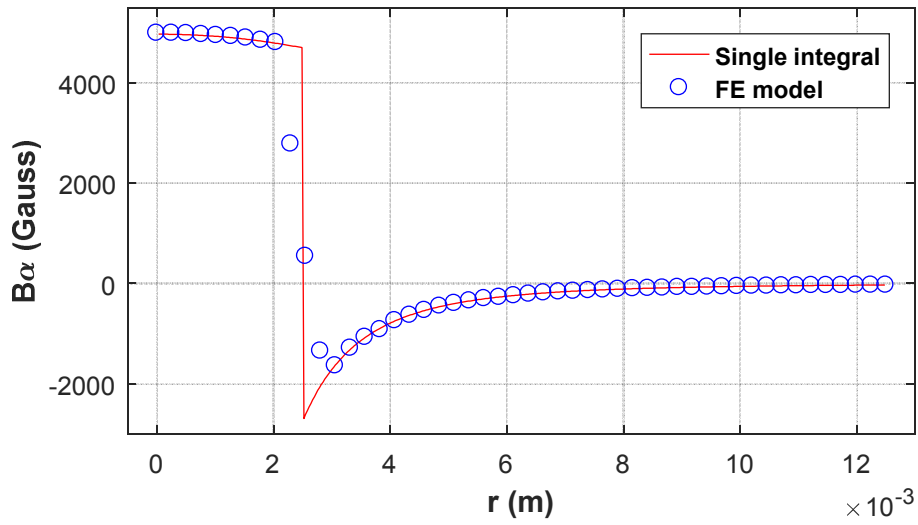
Fig. 4.6 Single integral vs FE model: Tangential component
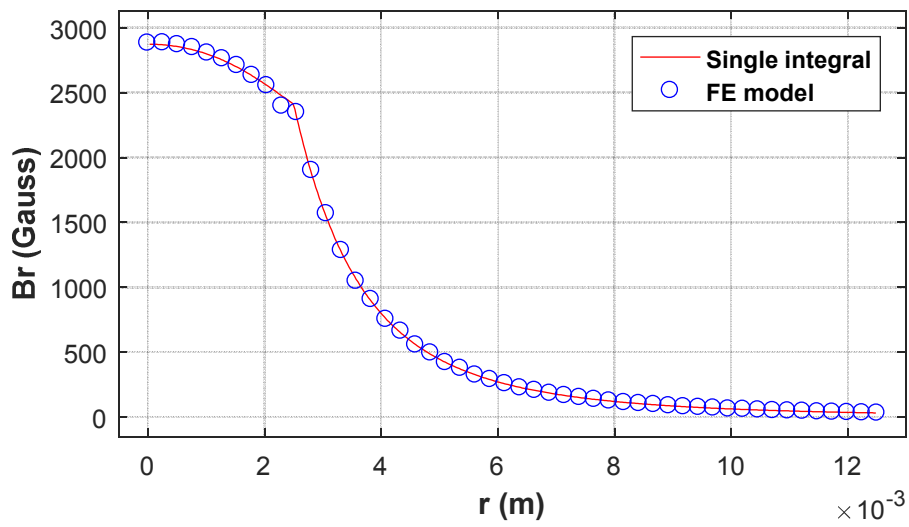
Fig. 4.7 Single integral vs FE model: Radial component

4.3 Derivation of the analytical expressions of the magnetic field generated by a permanent magnet with diametrical magnetization

With the help of MATHEMATICA® to analytically solve the above derived single integral expressions (Eqs. 4.3, 4.4, 4.5 and 4.5.1), the analytical expressions of the axial, azimuthal and radial components of the magnetic field were obtained as follows:

4.3.1 The axial component

Table 4.2 Parameters used in Eq. (4.6)

Parameters	Definition
a	$\left(z_K - \dfrac{h}{2}\right)^2 + R^2 + r^2$
b	$\left(z_K + \dfrac{h}{2}\right)^2 + R^2 + r^2$
c	$2Rr$
p	$\dfrac{2c}{c - a}$
u	$\dfrac{2c}{c - b}$

The analytical expression of the axial component $H_{K(z)}^{(3D)}(r, \alpha, z_K)$ was obtained with the parameters illustrated in Table 4.2:

$$H_{K(z)}^{(3D)}(r, \alpha, z_K) = \frac{JR\sin\alpha}{\pi\mu_0}\left(\frac{(a\mathbf{K}[p] + (c - a)\mathbf{E}[p])}{c\sqrt{a - c}} - \frac{(b\mathbf{K}[u] + (c - b)\mathbf{E}[u])}{c\sqrt{b - c}}\right) \qquad (4.6)$$

Here, $\mathbf{K}[m] = \int_0^{\frac{\pi}{2}} \frac{d\theta}{\sqrt{1 - m\sin^2\theta}}$ is the complete elliptic integral of the first kind,   (4.6a)

$\mathbf{E}[m] = \int_0^{\frac{\pi}{2}} \sqrt{1 - m\sin^2\theta}$ is the complete elliptic integral of the second kind.   (4.6b)

4.3.2 The azimuthal component

Table 4.3 Parameters used in Eq. (4.7) and Eq. (4.8)

Parameters	Definition
a	$R^2 + r^2$
b	$2Rr$
c	$\dfrac{h}{2} - z_K$
d	$\dfrac{h}{2} + z_K$
t	$\cos\beta$
ζ	$\sqrt{1 - t^2}$
η	$\sqrt{\dfrac{b(t + 1)}{a + b + c^2}}$
κ	$\sqrt{\dfrac{b(t - 1)}{a - b + c^2}}$

λ	$\sqrt{\dfrac{a - bt + c^2}{a + b + c^2}}$
ν	$\text{ArcSin}\left[\dfrac{\sqrt{t + 1}}{\sqrt{2}}\right]$
ξ	$\dfrac{2b}{c^2 + a + b}$
ς	$\dfrac{2b}{a + b}$
χ	$\text{ArcSin}\left[\sqrt{\dfrac{c^2 + a - bt}{c^2 + a + b}}\right]$
ψ	$\dfrac{c^2 + a + b}{c^2 + a - b}$
Υ	$\dfrac{4r^2}{c^2 + 4r^2}$

The analytical expression of the tangential component $H^{(3D)}_{K(\alpha)}(r, \alpha, z_K)$ was obtained with the parameters illustrated in Table 4.3 as follows:

$$H^{(3D)}_{K(\alpha)}(r, \alpha, z_K) = \frac{JR^2\cos\alpha}{2\pi\mu_0}\left(\delta(t_2,a,b,c) - \delta(t_1,a,b,c) + \delta(t_2,a,b,d) - \delta(t_1,a,b,d)\right) \quad (4.7)$$

where, the auxiliary function δ is as follows:

$$\delta(t,a,b,c) = -\frac{2c\lambda}{b^2\varsigma\sqrt{a\text{-}bt+c^2}}\left(-a\varsigma\mathbf{F}[\nu,\xi]+(a\text{-}b)\varsigma\mathbf{Pi}[\varsigma,\nu,\xi]+(t+1)b\kappa\mathbf{F}[\chi,\psi]+(t+1)\left(-(-a+b-c^2)\right)\kappa\mathbf{E}[\chi,\psi]\right);$$

Here, $\mathbf{F}[\varphi, m] = \int_0^\varphi \dfrac{d\theta}{\sqrt{1-m\sin^2\theta}}$ is the incomplete elliptic integral of the first kind,   (4.7a)

$\mathbf{E}[\varphi, m] = \int_0^\varphi \sqrt{1-m\sin^2\theta}$ is the incomplete elliptic integral of the second kind,   (4.7b)

$\mathbf{Pi}[n, \varphi, m] = \int_0^\varphi \dfrac{d\theta}{\left(1-n\sin^2\theta\right)\sqrt{1-m\sin^2\theta}}$ is the incomplete elliptic integral of the third kind. (4.7c)

4.3.3 The radial component

The analytical expression of the radial component $H_{K(r)}^{(3D)}(r, \alpha, z_K)$ was obtained with parameters, as illustrated in Table 4.3:

$H_{K(r)}^{(3D)}(r, \alpha, z_K) =$

$\dfrac{JR\sin\alpha}{2\pi\mu_0}\big(\gamma(t_2,a,b,c,r,R) - \gamma(t_1,a,b,c,r,R) + \gamma(t_2,a,b,d,r,R) - \gamma(t_1,a,b,d,r,R)\big)$ (4.8)

where, the auxiliary function γ is as follows:

$\gamma(t,a,b,c,r,R) = \big(2c\lambda\big((a + b)(a - b + c^2)R\kappa(1 + t)\mathbf{E}[\chi, \psi] + (a + b)(br -$

$aR)\eta\zeta\mathbf{F}[v, \xi] + (a + b + at + bt)bR\kappa\mathbf{F}[\chi, \psi] + (aR - br)a\eta\zeta\mathbf{Pi}[\varsigma, v, \xi]\big)/\big(\eta\zeta b^2(a +$

$b)\sqrt{a + c^2 - bt}\big);$

For the point K on the cylindrical surface, or when $r = R$, the radial component can be calculated as follows:

$$H_{K(r)}^{(3D)} \, (r = R, \, \alpha, \, z_K) = \frac{J\sin\alpha}{4\pi\mu_0} \big(c f(r,c) + d f(r,d) \big) \qquad (4.8a)$$

where, the auxiliary function f is expressed as follows:

$$f(r,c) = \frac{(c^2+2r^2)\mathbf{K}[\Upsilon] - (c^2+4r^2)\mathbf{E}[\Upsilon]}{r^2 \sqrt{c^2+4r^2}}$$

The complete elliptic integrals of the first and second kinds $\mathbf{K}[m]$, $\mathbf{E}[m]$ are calculated using Eq. (4.6a) and Eq. (4.6b).

The incomplete elliptic integrals of the first, second and third kinds $\mathbf{F}$, $\mathbf{E}$ and $\mathbf{Pi}$ are calculated using Eqs. (4.7a), (4.7b) and (4.7c).

The values of t_1 and t_2 in Eq. (4.7) and Eq. (4.8) can be set to be 0.999999999 or closer to 1 and -0.999999999 or closer to -1 respectively to avoid indefinite values, whilst evaluating the expressions.

4.4 Calculation of the magnetic field created by a diametrically magnetized ring shaped permanent magnet

For a ring shaped permanent magnet with the parameters shown in Fig. 4.8, its inner radius is R_{in}; its outer radius is R_{out}; its thickness is h; its magnetization $\mathbf{J}$ is assumed to be uniformly diametrical and along axis Y, the magnetic field $\mathbf{H}_K(\text{ring})$ at point K can be computed using the principle of superposition Eq. (4.9):
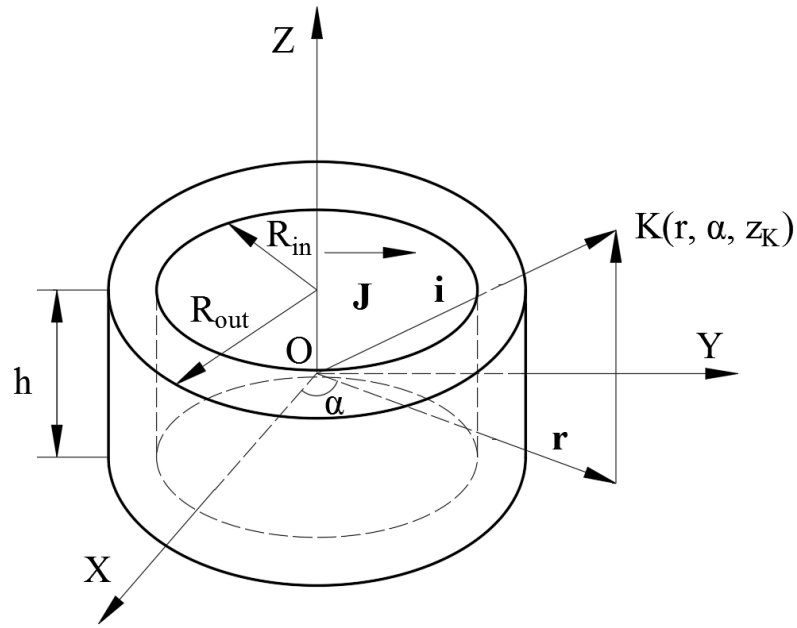
Fig. 4.8 Diametrically magnetized ring shaped permanent magnet

$$\mathbf{H}_K(\text{ring}) = \mathbf{H}_K(R_{out}) - \mathbf{H}_K(R_{in}) \qquad (4.9)$$

where $\mathbf{H}_K(R_{out})$ is the magnetic field at point K created by a cylinder with the radius R_{out} and $\mathbf{H}_K(R_{in})$ is the magnetic field at point K created by another cylinder with the radius R_{in}. These two cylinders have the same $\mathbf{J}$ and thickness as those of the ring. Using the above expressions from Eq. (4.6) to Eq. (4.8), the axial, azimuthal and radial components of the magnetic field of a diametrically magnetized ring shaped permanent magnet can be calculated.

Knowing the magnetic field intensity, the magnetic flux density can be computed as follows:

$$\mathbf{B}_K = \mu_0 \mathbf{H}_K \qquad \text{(in the air space)} \qquad (4.9)$$

and
$$\mathbf{B}_K = \mu_0 \mathbf{H}_K + \mathbf{J} \qquad \text{(inside the magnet)} \qquad (4.10)$$

Chapter 5

Verification results of the derived analytical expressions of the magnetic field generated by a permanent magnet with diametrical magnetization

The developed analytical expressions (Eq. (4.6) to Eq. (4.8)) were implemented in MATLAB R2016b of MATHWORKS to calculate the axial, azimuthal and radial components of the magnetic flux density, both in the air space and inside the magnet, generated by a cylinder diametrically magnetised rare earth permanent magnet (Figs. 4.1 and 4.2) with a radius $R = 2.5$ mm and thickness $h = 5$ mm; and magnetic remanence $J = 1$ T, which is generated by a scalar coercivity of 800000 A.m^{-1} [42]. The Finite Element Analysis was carried out using Electromagnetic simulation software (EMS) from EMWORKS and integrated with 3D CAD INVENTOR software from AUTODESK.

The error between the results of the analytical expressions ($B_{Analytical}$) and those of the Finite Element (FE) model ($B_{FE\ model}$) is calculated using Eq. (5.1)

$$\text{Error} = \left| \frac{B_{Analytical} - B_{FE\ model}}{B_{FE\ model}} \right| \times 100\ \% \qquad (5.1)$$

In Figs. 3(a), 4(a) and 5(a), the magnetic field components are presented with a solid line for those computed using the derived analytical expressions of this paper, with circles for those computed using the FE model and with a dotted line for those computed using the model by Caciagli et al [42]. In Fig. 5.2, 5.4 and 5.6, the errors are presented with a solid line for those derived from the analytical expression of this paper, and with a dashed line for those derived from the model by Caciagli et al. [42].

*Table 5.1 Errors of the analytical model derived in this paper and those of Caciagli et al [42] tested against the Finite Element (FE) model with r in the interval from 0 mm to 12.5 mm: * denotes the errors inside the magnet, ** denotes the errors in the air space*

Components of the magnetic field	Maximum error (%)				Average error (%)				Minimum error (%)			
	Model derived in this paper		Model by Caciagli et al. [42]		Model derived in this paper		Model by Caciagli et al. [42]		Model derived in this paper		Model by Caciagli et al. [42]	
	*	**	*	**	*	**	*	**	*	**	*	**
Axial component	28.9	5.4	916.5	154	less than 2.5	less than 2	362.2	97.9	0.068	0.16	47.1	39.1
Azimuthal component	0.16	3.36	828.5	254.9	less than 0.16	less than 1.5	249.4	112	0.007	0.49	24.04	34.24
Radial component	0.2	1.8	819.7	174.3	less than 0.2	less than 1.5	237.8	91.2	0.005	0.002	2.6	47.67

Table 5.2 Computational times

Components of the magnetic field	Time-consumption (seconds)		
	Double integration model [19]	Analytical model in this paper	Analytical model by Caciagli et al. [42]
Axial component	0.33	4.6×10^{-3}	0.08×10^{-3}
Azimuthal component	0.045	0.15	0.018
Radial component	0.24	0.15	0.018
Total	0.615	0.3046	0.03608

Table 5.3 Comparison of the axial component of the magnetic field computed by the analytical model derived in this paper and those of double integration form [19]

Computed points K(r mm, α^o, z mm)	Analytical model in this paper	Double integration model [19]
(1, 30º,1)	2.157769964794315e+02	2.157769964794310e+02
(2,60º,1)	6.708086824080323e+02	6.708086824080297e+02
(2,90º,2)	2.090489643938749e+03	2.090489643938752e+03
(3,60º,2)	1.642034971824546e+03	1.642034971824547e+03
(7,45º,3)	1.285267148068441e+02	1.285267148068443e+02
(8,45º,2)	64.672428644072369	64.672428644071971
(9,0º,3)	0	-1.663901291691562e-14 when the integration increment is increased to the square root of the minimum; indefinite with the minimum integration increment

Table 5.4 Comparison of the azimuthal component of the magnetic field computed by the analytical model derived in this paper and those of double integration form [19]

Computed points K(r mm, α°, z mm)	Analytical model in this paper	Double integration model [19]
(1, 30°,1)	2.075341353118272e+03	2.075342030279546e+03
(2,60°,1)	6.883383752352425e+03	6.883383655587118e+03
(2,90°,2)	10000	10000 when the integration increment is increased to the square root of the minimum; indefinite with the minimum integration increment
(3,60°,2)	-9.414782387941905e+02	-9.414783284170040e+02
(7,45°,3)	-1.249742783341035e+02	-1.249742322552511e+02
(8,45°,2)	-97.645377896016626	-97.645374376110695
(9,0°,3)	-91.127178430913247	-91.127228807875156

Table 5.5 Comparison of the radial component of the magnetic field computed by the analytical model derived in this paper and those of double integration form [19]

Computed points K(r mm, α°, z mm)	Analytical model in this paper	Double integration model [19]
(1, 30°,1)	3.254215441314990e+03	3.254090873644084e+03
(2,60°,1)	5.171522650531067e+03	5.170893368858451e+03
(2,90°,2)	6.548622537747931e+03	6.547984542927014e+03
(3,60°,2)	2.665756882192566e+03	2.666260855598413e+03
(7,45°,3)	1.951738642613515e+02	1.951864669091654e+02
(8,45°,2)	1.772092192324710e+02	1.772204783074605e+02
(9,0°,3)	0	-5.507071531793312e-14 when the integration increment is increased to the square root of the minimum; indefinite with the minimum integration increment

Figs. 5.1 and 5.2 show that the developed analytical expressions can compute the magnetic field precisely, with an average error of less than 2.5 % for the axial component inside the magnet, except for the field point near the centre of the cylinder (the radial distance r is less than 1 mm) where the error is up to 30%. This could be due to the mesh-based approach of the finite-element solver [42], for example, the mesh could not be fine enough to yield exact results such as some nodes of the calculated point were located in the negative field when the point is close to the centre of the cylinder. The average error decreases to below 2% in the air space and it continues to decline with the increase in the radial distances. In contrast, the model developed by Caciagli et al [42] yields inaccurate results with a minimum error of 39.1 % and this error increases for the other field points inside the magnet and in the air space. Figs. 5.3, 5.4, 5.5 and 5.6 show that using the derived analytical expressions, the average errors are lower than 0.2 % for the azimuthal and radial components inside the magnet. The errors increase for the magnetic field close to the cylindrical surface of the magnet ($r \approx R$), where a discontinuity of the magnetic field is observed (Fig. 5.3 and Fig. 5.5 show the discontinuity value of the radial component can be calculated using Eq. 4.5.1). This is, however, as mentioned before, due to the mesh-based approach of the finite-element solver [42]. The average errors of these components drop below 1.5 % for the field points in the air space and they keep decreasing with the increase in the radial distances. On the other hand, using the model by Caciagli et al. [42] produces a minimum error of 24.04 % for the azimuthal component and 2.6 % for radial component and they go up for the other field points both inside the magnet and in the air space. The inaccuracy of the model by Caciagli et al [42] can be explained, as, in the derivation steps, the

magnetic scalar potential was approximately presented with the complete elliptic integrals. Then, the final expressions were derived by taking derivatives of this scalar potential directly, which causes the error when using them to compute the magnetic field. Table 5.1 presents more details about the maximum, average and minimum errors of the analytical model derived in this paper and those by Caciagli et al [42].

Evaluated in MATLAB R2016b with the minimum integration increment (double precision in MATLAB), using the analytical expression derived in this paper, it took an average of 4.6 milliseconds on a personal computer (with Processor Intel® Core™ i7-6700 CPU @ 3.40 GHz 3.40 GHz) to calculate the axial component at a single location (2000 samples with random input variables). It took less than 0.2 seconds to compute the azimuthal and radial components. On the other hand, using the analytical model by Caciagli et al. [42] in the same configuration, it took 0.08 milliseconds to calculate the axial component and less than 0.02 seconds to compute the azimuthal and radial components. Even though Caciagli's analytical model computes slightly faster than the work presented in this paper, the results of the work presented are far more accurate. Evaluated in MATLAB with the same configuration as mentioned above, the double integration of the axial component (from Eq. (4.2)) took 0.33 seconds, the double integration of the azimuthal component took 0.045 seconds and the double integration of the radial component took 0.24 seconds (Table 5.2). This can demonstrate that the analytical model derived in this study outperforms the double integration expression [19] in terms of the computational cost but remains very close in terms of the calculated results in most of the randomly selected points (Table 5.3, 5.4 and 5.5).
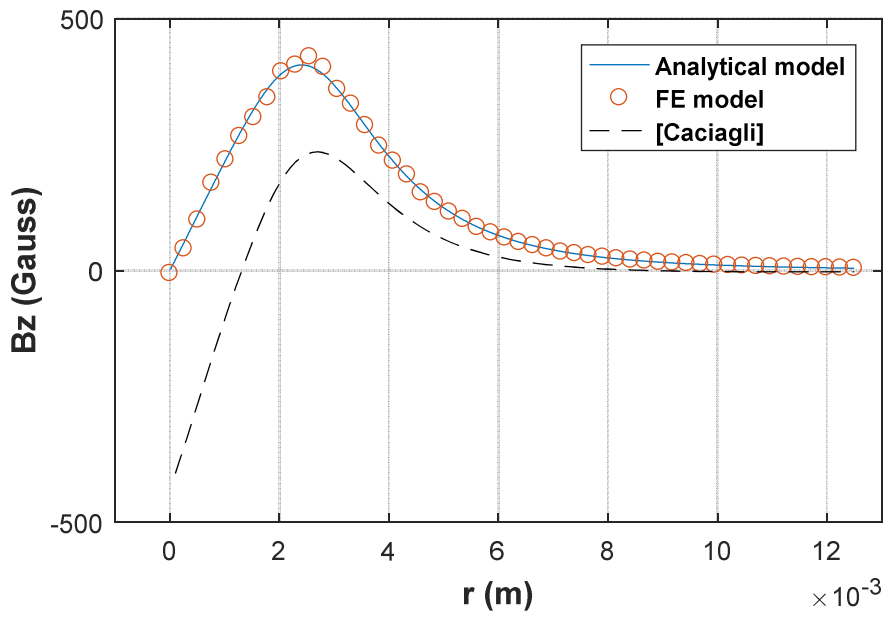
Fig. 5.1 Axial component of the magnetic field: Magnetic field
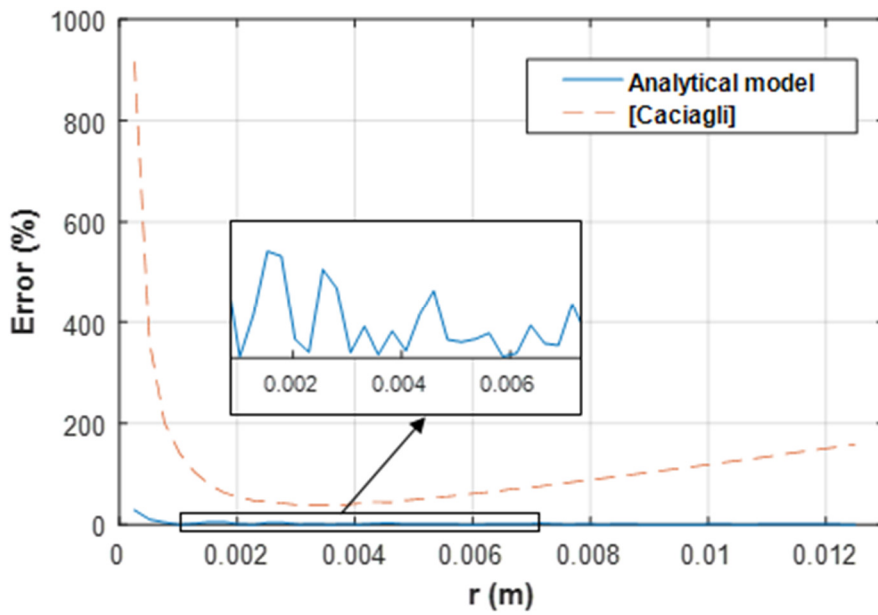
Fig. 5.2 Axial component of the magnetic field: Error rates between the analytical models and the FE
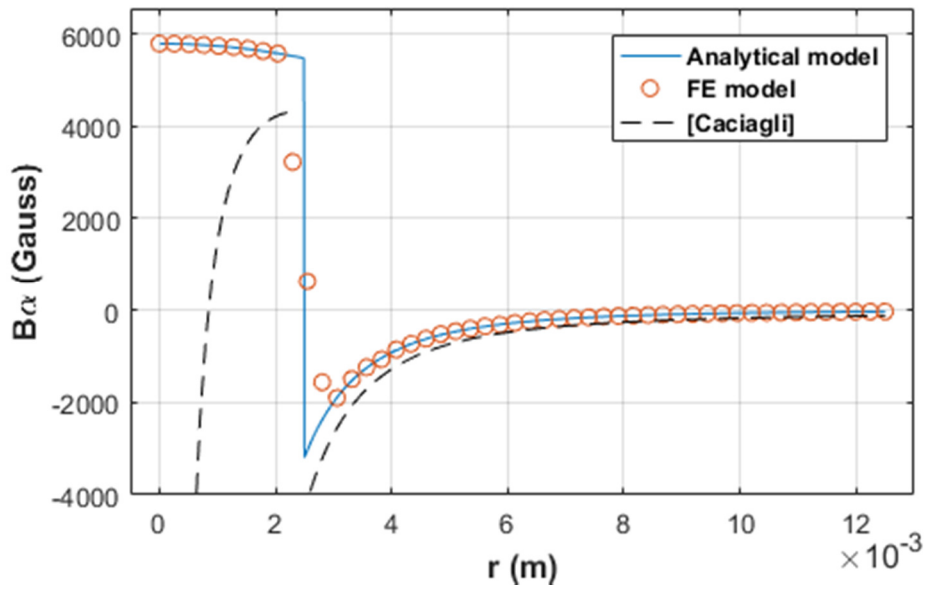
model

Fig. 5.3 Azimuthal component of the magnetic field: Magnetic field
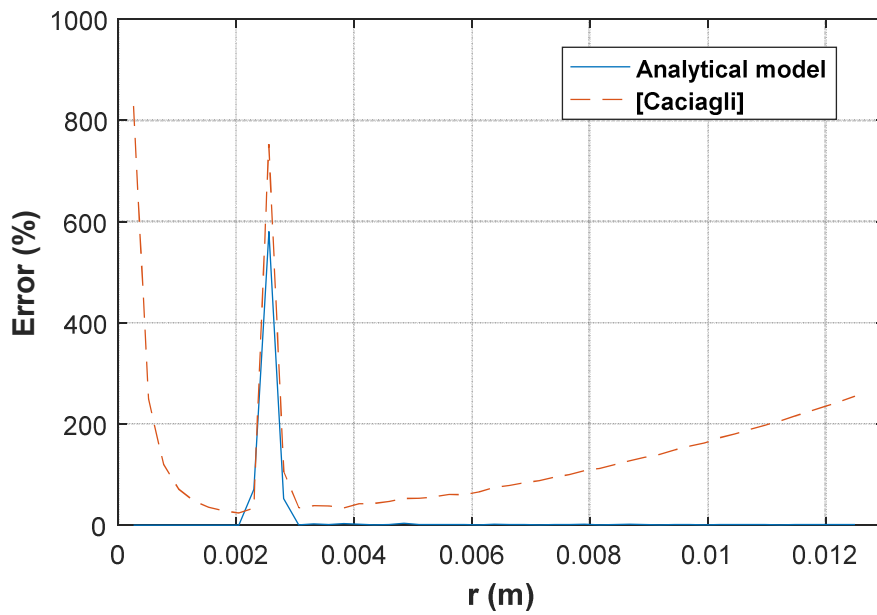
Fig. 5.4 Azimuthal component of the magnetic field: Error rates between the analytical models and the FE model
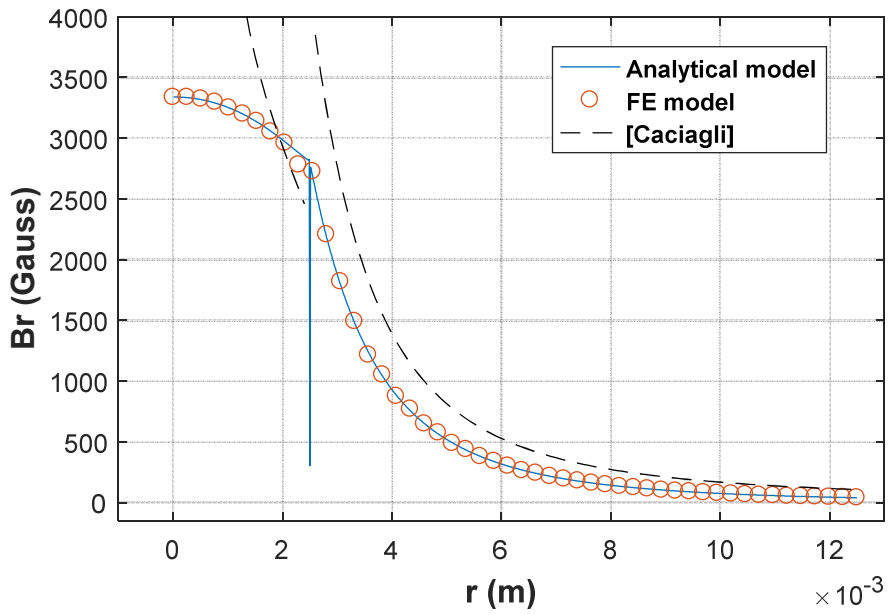
Fig. 5.5 Radial component of the magnetic field: Magnetic field
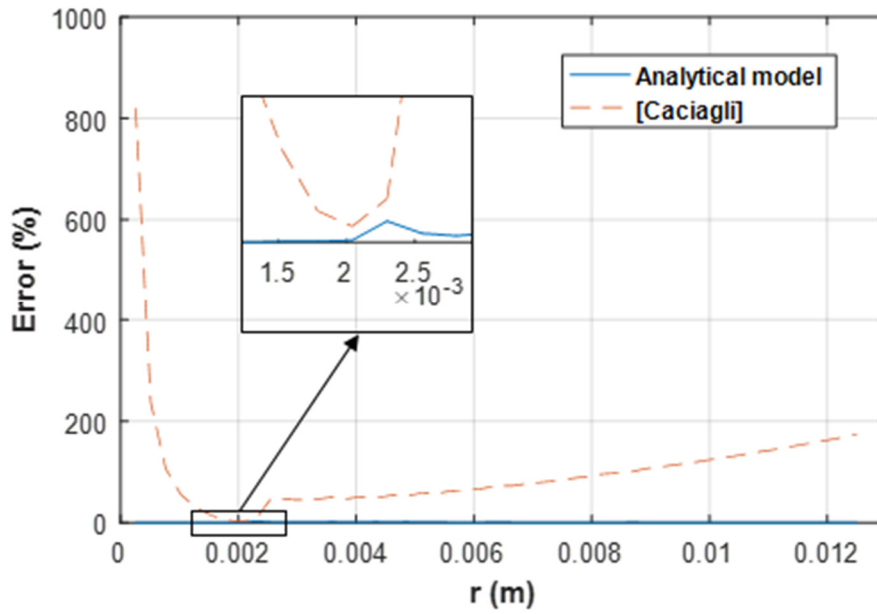
Fig. 5.6 Radial component of the magnetic field: Error rates between the analytical models and the FE model

Chapter 6

Conclusion and future work

An exact analytical model to compute the magnetic field generated by a diametrically magnetised cylindrical/ring shaped permanent magnet with a limited length, at any point in 3D space, both inside the magnet and in the air, was developed in this thesis. Based on geometrical and analytical analyses, without any approximation in the derivation steps, the magnetic field is expressed analytically using the complete elliptic integrals for its axial component and incomplete elliptic integrals for its azimuthal and radial components. The total computational cost of the analytical model is lower than that of a double integration model while the two models are in very good agreement in terms of computed results. The results of the developed analytical expressions are in good agreement with those using Finite Element Analysis and far more precise than those obtained by Caciagli et al. [42].

In the future, the derived analytical expressions will be further implemented to optimize the permanent magnet's parameters and to define the optimized air gap between the magnet and the Hall effect sensors used in the study proposed by the authors [39].

References

[1] R. Ravaud, G. Lemarquand, V. Lemarquand and C. Depollier, "Permanent magnet couplings: Field and torque three-dimensional expressions based on the Coulombian model," *IEEE Transactions on Magnetics*, vol. 45, no. 4, pp. 1950-1958, Apr. 2009.

[2] O. Cuguat, J. Delamare, and G. Reyne, "Magnetic micro-actuators and systems (magmas)," *IEEE Transactions on Magnetics*, vol. 39, no. 5, pp. 3607–3612, Sep. 2003.

[3] J. Wang, G. W. Jewell, and D. Howe, "Design optimisation and comparison of tubular permanent magnet machines topologies," *IEE Proceedings - Electric Power Applications*, vol. 148, pp. 456–464, 2001.

[4] J. F. Charpentier and G. Lemarquand, "Optimization of unconventional p.m. couplings," *IEEE Transactions on Magnetics*, vol. 38, no. 2, pp. 1093–1096, Mar. 2002.

[5] V. Lemarquand, J. F. Charpentier, and G. Lemarquand, "Nonsinusoidal torque of permanent-magnet couplings," *IEEE Transactions on Magnetics*, vol. 35, no. 5, pp. 4200–4205, Sep. 1999.

[6] M. Berkouk, V. Lemarquand, and G. Lemarquand, "Analytical calculation of ironless loudspeaker motors," *IEEE Transactions on Magnetics*, vol. 37, no. 2, pp. 1011–1014, Mar. 2001.

[7]   O. M. Kwon, C. Surussavadee, M. Chari, S. Salon, and K. Vasubramaniam, "Analysis of the far field of permanent magnet motors and effects of geometric asymmetries and unbalance in magnet design," *IEEE Transactions on Magnetics*, vol. 40, no. 3, pp. 435-442, May 2004.

[8]   E. Paperno, I. Sasada, and E. Leonovich, "A new method for magnetic position and orientation tracking," *IEEE Transactions on Magnetics*, vol. 37, no. 4, pp. 1938–1940, Jul. 2001.

[9]   T. W. R. Fountain, P. V. Kailat, and J. J. Abbott, "Wireless control of magnetic helical microrobots using a rotating-permanent-magnet manipulator," *Proceedings of IEEE International Conference on Robotics and Automation,* pp. 576–581, 2010.

[10]   S.-T. Wu, J.-Y. Chen, and S.-H. Wu, "A rotary encoder with an eccentrically mounted ring magnet," *IEEE Transactions on Instrumentation and Measurement*, vol. 63, no. 8, pp. 1907–1915, Aug. 2014.

[11]   K. Ng, Z. Q. Zhu and D. Howe, "Open-circuit field distribution in a brushless motor with diametrically magnetised PM rotor, accounting for slotting and eddy current effects," *IEEE Transactions on Magnetics*, vol. 32, no. 5, pp. 5070-5072, 1996.

[12]   G. Eid and A. Mouillet, "Transistorized dc brushless micromotor with rare-earth permanent magnets," *Proceddings of the International Conference on Electrical Machines*, pp. 570-573, 1984.

[13] S. M. Jang, M. M. Koo, Y. S. Park, J. Y. Choi and S. H. Lee, "Characteristic analysis on permanent magnet synchronous machines with three types of diametrically magnetized rotors under magnetic circuit construction conditions," *Proceedings of IEEE Vehicle Power and Propulsion Conference*, pp. 227-230, 2012.

[14] S. M. Jang, J. Y. Choi, D. J. You and H. S. Yang, "Electromagnetic analysis of high speed machines with diametrically magnetized rotor considering slotting effect and applied to new magnetization modelling, " *Proceedings of IEEE International Conference on Electric Machines and Drives*, pp. 1204-1211, 2005.

[15] G. Lemarquand and V. Lemarquand, "Annular magnet position sensor," *IEEE Transactions on Magnetics*, vol. 26, no. 5, pp. 2041-2043, 1990.

[16] S. Wang, J. Jin, T. Li and G. Liu, "High-accuracy magnetic rotary encoder," *System Simulation and Scientific Computing*, pp. 74-82, 2012.

[17] Y. Y. Lee, R. H. Wu and S. T. Xu, "Applications of linear Hall-effect sensors on angular measurement," *IEEE International Conference on Control Applications (CCA)*, pp. 479-482, 2011.

[18] Y. Smirnov, T. Kozina, E. Yurasova and A. Sokolov, "Analog-to-Digital converters of the components of a displacement with the use of microelectronic sine-cosine magnetic encoders," *Measurement Techniques*, vol. 57, pp. 41-46, 2014.

[19]   M. Fontana, F. Salsedo and M. Bergamasco, "Novel magnetic sensing approach with improved linearity," *Sensors*, no. 6, pp. 7618-7632, 2013.

[20]   B. Lenzo, M. Fontana, S. Marcheschi, F. Salsedo, A. Frisoli and M. Bergamasco, "Trackhold: A novel passive arm-support device," *ASME Journal of Mechanisms and Robotics*, vol. 8, pp. 1-9, 2015

[21]   M. H. Rahman, C. O. Luna, M. Saad and P. Archambault, "EMG based control of a robotic exoskeleton for shoulder and elbow motion assist," *Jounal of Automation and Control Engineering*, vol. 3, no. 4, pp. 270-276, Aug. 2015.

[22]   K. Kiguchi and Y. Hayashi, "An EMG-based control for an upper-limb power-assist exoskeleton robot," *IEEE Transactions on Systems, Man, and Cybernetics, Part B (Cybernetics)*, vol. 42, no. 4, pp. 1064-1071, Aug. 2012.

[23]   D. S. Andreasen, S. K. Alien and D. A. Backus, "Exoskeleton with EMG based active assistance for rehabilitation," *Proceedings of the 9th International Conference on Rehabilitation Robotics*, pp. 333-336, 2005.

[24]   T. Lenzi, S. M. M. De Rossi, N. Vitiello and M. C. Carrozza, "Intention-based EMG control for powered exoskeletons," *IEEE Transactions on Biomedical Engineering*, vol. 59, no. 8, pp. 2180-2190, Aug. 2012.

[25]   M. H. Rahman, C. O. Luna, M. Saad and P. Archambault, "Motion control of an exoskeleton robot using electromyogram signals," *Proceedings of the International Conference on Mechatronics and Robotics, Structural Analysis*, Merosta, 2014.

[26] K. Kiguchi, T. Tanaka and T. Fukuda, "Neuro-fuzzy control of a robotic exoskeleton with EMG signals," *IEEE Transactions on Fuzzy Systems*, vol. 12, no. 4, pp. 481-490, Aug. 2004.

[27] T. Noda, N. Sugimoto, J. Furukawa, M. A. Sato, S. H. Hyon and J. Morimoto, "Brain-controlled exoskeleton robot for BMI rehabilitation," *Proceedings of the 12th IEEE-RAS International Conference on Humanoid Robots (Humanoids)*, Osaka, pp. 21-27, 2012.

[28] D. C. Irimia, M. S. Poboroniuc, F. Serea, A. Baciu and R. Olaru, "Controlling a FES-EXOSKELETON rehabilitation system by means of brain-computer interface," *Proceedings of the International Conference and Exposition on Electrical and Power Engineering (EPE),* Iasi, pp. 352-355, 2016.

[29] T. D. Lalitharatne, K. Teramoto, Y. Hayashi, K. Tamura and K. Kiguchi, "EEG-based evaluation for perception-assist in upper-limb power-assist exoskeletons," *Proceedings of the World Automation Congress (WAC)*, Waikoloa, HI, pp. 307-312, 2014.

[30] A. Kilicarslan, S. Prasad, R. G. Grossman and J. L. Contreras-Vidal, "High accuracy decoding of user intentions using EEG to control a lower-body exoskeleton," *Proceedings of the 35th Annual International Conference of the IEEE Engineering in Medicine and Biology Society (EMBC)*, Osaka, pp. 5606-5609, 2013.

[31]   K. Lee, D. Liu, L. Perroud, R. Chavarriaga and J. del R. Millán, "A brain-controlled exoskeleton with cascaded event-related desynchronization classifiers," *Robotics and Autonomous Systems*, vol. 90, pp. 15-23, Apr. 2017.

[32]   Z. Li, W. He, C. Yang, S. Qiu, L. Zhang and C. Y. Su, "Teleoperation control of an exoskeleton robot using brain machine interface and visual compressive sensing," *Proceedings of the 12th World Congress on Intelligent Control and Automation (WCICA),* Guilin, pp. 1550-1555, 2016.

[33]   C. Vidaurre, C. Klauer, T. Schauer, A. R. Murguialday and K. R. Müller, "EEG-based BCI for the linear control of an upper-limb neuroprosthesis," *Medical Engineering & Physics*, vol. 38, pp. 1195-1204, 2016.

[34]   L. I. Ammar, B. Y. Kaddouh, M. K. Mohanna and I. H. Elhajj,   "SAS: SMA aiding sleeve," *Proceedings of IEEE International Conference on Robotics and Biomechatronics*, Tianjin, pp. 1596-1599, 2010.

[35]   M. R. U. Islam and S. Bai, "Intention detection for dexterous human arm motion with FSR sensor bands," *Proceedings of the Companion of the 2017 ACM/IEEE International Conference on Human-Robot Interaction*, Vienna, Austria, pp. 139-140, 2017.

[36]   Z. G. Xiao, A. M. Elnady and C. Menon, "Control an exoskeleton for forearm rotation using FMG," *Proceedings of the 5th IEEE RAS & EMBS International Conference on Biomedical Robotics and Biomechatronics*, Sao Paulo, pp. 591-596, 2014.

[37]   E. Cho, R. Chen, L.-K. Merhi, Z. Xiao, B. Pousett and C. Menon, "Force myography to control robotic upper extremity prostheses: A feasibility study," *Frontiers in Bioengineering and Biotechnology*, vol. 4, 2016.

[38]   J. Huang, W. Huo, W. Xu, S. Mohammed and Y. Amirat,   "Control of upper-limb power-assist exoskeleton using a human-robot interface based on motion intention recognition," *IEEE Transactions on Automation Science and Engineering.*, vol. 12, no. 4, pp. 1257-1270, Oct. 2015.

[39]   V. T. Nguyen, T. -F. Lu and P. Grimshaw, "Human intention recognition based on contact-less sensors to control an elbow and forearm assistive exoskeleton," *Proceedings of the 7th International Conference of Asian Society for Precision Engineering and Nanotechnology (ASPEN 2017)*, ARM-P-06, Seoul, Korea, Nov. 2017.

[40]   V.Schaller, U. Kräling, C. Rusu, K. Petersson, J. Wipenmyr, A. Krozer, G. Wahnström,   A. Sanz-Velasco, P. Enoksson and C. Johansson, "Motion of nanometer sized magnetic particles in a magnetic field gradient," Journal of Applied Physics, vol. 104, pp. 093918-(1 -14), 2008.

[41]   K . Warnke, "Finite-element modelling of the separation of magnetic microparticles in fluid," *IEEE Transactions on Magnetics*, vol. 39, no. 3, pp. 1771-1777, May 2003.

[42]   A. Caciagli, R. J. Baars, A. P. Philipse and B. W. M. Kuipers, "Exact expression for the magnetic field of a finite cylinder with arbitrary uniform magnetization,"

Journal of Magnetism and Magnetic Materials, vol. 456, pp. 423-432, June 2018.

[43]   W. Robertson, B. Cazzolato and A. Zander, "A simplified force equation for coaxial cylindrical magnets and thin coils," *IEEE Transactions on Magnetics*, vol. 47, no. 8, pp. 2045-2049, 2011.

[44]   E. P. Furlani, "Permanent Magnet and Electromechanical Devices: Materials, Analysis and Applications," Academic Press, 2001.

[45]   H. L. Rakotoarison, J. P. Yonnet and B. Delinchant,   "Using Coulombian approach for modeling scalar potential and magnetic field of a permanent magnet with radial polarization," *IEEE Transactions on Magnetics*, vol. 43, no. 4, pp. 1261-1264, 2007.

[46]   R. Ravaud and G. Lemarquand,"Comparison of the Coulombian and Amperian current models for calculating the magnetic field produced by radially magnetized arc-shaped permanent magnets," *Progress in Electromagnetics Research*, PIER 95, pp. 309-327, 2009.

[47]   R. Ravaud, G. Lemarquand, V. Lemarquand and C. Depollier, "Analytical calculation of the magnetic field created by permanent-magnet rings," *IEEE Transactions on Magnetics*, vol. 44, no. 8, pp. 1982-1989, 2008.

[48]   S. I. Babic and C. Akyel, "Improvement in the analytical calculation of the magnetic field produced by permanent magnet rings," *Progress in Electromagnetics Research C*, vol. 5, pp. 71-82, 2008.

[49] R. Ravaud, G. Lemarquand, V. Lemarquand and C. Depollier, "The three exact components of the magnetic field created by a radially magnetized tile permanent magnet," *Progress in Electromagnetics Research*, PIER 88, pp. 307-319, 2008.

[50] R. Ravaud, G. Lemarquand, V. Lemarquand, and C. Depollier, "Magnetic field produced by a tile permanent magnet whose polarization is both uniform and tangential," *Progress In Electromagnetics Research B*, Vol. 13, 1-20, 2009.

[51] R. Ravaud and G. Lemarquand, "Analytical expression of the magnetic field created by tile permanent magnets tangentially magnetized and radial currents in massive disks," *Progress In Electromagnetics Research B*, vol. 13, 309-328, 2009.

[52] T. Fukushima, "Precise, compact, and fast computation of complete elliptic integrals by piecewise minimax rational function approximation," *Journal of Computational and Applied Mathematics*, vol. 282, pp. 71–76, 2015.

[53] T. Fukushima, "Fast computation of incomplete elliptic integral of first kind by half argument transformation," *Numerische Mathematik,* vol. 116, pp. 687–719, 2010.

[54] T. Fukushima, "Precise and fast computation of a general incomplete elliptic integral of second kind by half and double argument transformations," *Journal of Computational and Applied Mathematics*, vol. 235, pp. 4140–4148, 2011.

[55] T. Fukushima, "Precise and fast computation of a general incomplete elliptic integral of third kind by half and double argument transformations," *Journal of Computational and Applied Mathematics*, vol. 236, pp. 1961-1975, 2012.

[56] J. Stratton, "Electromagnetic theory," McGraw-Hill book company, New York and London, 1941.

[57] J. Oberteuffer, "Magnetic separation: a review of principles, devices, and applications," *IEEE Transactions on Magnetics,* vol. 10, no. 2, pp. 223-238, 1974.

[58] G. Wysin, "Demagnetization fields," available on https://www.phys.ksu.edu/personal/wysin/notes/demag.pdf.

[59] G. B. Arfken and H. J Weber, "Mathematical methods for physicists," Academic Press, 2005.

[60] A. E. Umemei, "Development and application of magnetic modelling to the design of power devices," PhD Thesis, 2010.

[61] Y. Liu, D. J. Sellmyer, "Handbook of advanced magnetic materials," Springer, 2006

[62] J. M. D. Coey, "Magnetism and magnetic materials," Cambridge University Press, 2009

[63] A. Nicolaides, "Electrical and Electronic Principles II," PASS Publications, London, 1996.

[64]   J. N. Reddy, "Introduction to the Finite Element Method," McGraw-Hill,

        1993

[65]   https://www.emworks.com.

Appendix A

Derivation steps

A.1 The axial component $H_{K(z)}^{(3D)}(r, \alpha, z_K)$

From Eq. (4.2), the axial component $H_{K(z)}^{(3D)}(r, \alpha, z_K)$ can be expressed as follows:

$$H_{K(z)}^{(3D)}(r, \alpha, z_K) = \frac{JR}{4\pi\mu_0} \int_{\beta=-\pi}^{\beta=\pi} \int_{z=-h/2}^{z=h/2} \frac{(z_K - z)}{\left(R^2 + r^2 - 2Rr\cos\beta + (z_K - z)^2\right)^{\frac{3}{2}}} \sin(\alpha + \beta) \, dz \, d\beta \qquad (A.1)$$

Integrating Eq. (A.1) based on z yields:

$$H_{K(z)}^{(3D)}(r, \alpha, z_K) = \left(\frac{JR}{4\pi\mu_0} \int_{\beta=-\pi}^{\beta=\pi} \frac{1}{\sqrt{(z_K - z)^2 + \left|\overrightarrow{P'K}\right|^2}} \Bigg|_{z=-\frac{h}{2}}^{z=\frac{h}{2}} \sin(\alpha + \beta) \, d\beta \right) \qquad (A.2)$$

Here, $\left|\overrightarrow{P'K}\right|^2 = R^2 + r^2 - 2Rr\cos(\beta)$ (A.2.1); expanding (A.2) produces:

$$H_{K(z)}^{(3D)}(r, \alpha, z_K) = \left(\frac{JR}{4\pi\mu_0} \int_{\beta=-\pi}^{\beta=\pi} \left(\frac{1}{\sqrt{\left(z_K - \frac{h}{2}\right)^2 + \left|\overrightarrow{P'K}\right|^2}} - \frac{1}{\sqrt{\left(z_K + \frac{h}{2}\right)^2 + \left|\overrightarrow{P'K}\right|^2}} \right) (\cos(\beta)\sin(\alpha) \right.$$
$$\left. + \sin(\beta)\cos(\alpha)) \, d\beta \right) \qquad (A.3)$$

93

with consideration of periodic odd/even functions in the interval [-π; π] in equation

(A.3), the axial component is finally expressed as follows:

$$
H_{K(z)}^{(3D)}(r, \alpha, z_K) = \left(\frac{JR}{4\pi\mu_0} \int_{\beta=-\pi}^{\beta=\pi} \left(\frac{1}{\sqrt{\left(\frac{h}{2} - z_K\right)^2 + \left|\overrightarrow{P'K}\right|^2}} \right. \right.
$$
$$
\left. \left. - \frac{1}{\sqrt{\left(\frac{h}{2} + z_K\right)^2 + \left|\overrightarrow{P'K}\right|^2}} \right) \cos(\beta) \, d\beta \right) \sin(\alpha) \qquad (A.4)
$$

For point K belonging to the symmetrical plane of the cylinder $z_K = 0$, expression

(A.4) can be simplified to $H_{K(z)}^{(Fontana)}(r, \alpha, z_K = 0) = 0$, which is presented in the study

by Fontana et al. [19].

A.2 The tangential (Azimuthal) component $H_{K(\alpha)}^{(3D)}(r, \alpha, z_K)$

From Eq. (4.2), $H_{K(\alpha)}^{(3D)}(r, \alpha, z)$ can be expressed as follows:

$$
H_{K(\alpha)}^{(3D)}(r, \alpha, z_K) = \frac{JR}{4\pi\mu_0} \int_{\beta=-\pi}^{\beta=\pi} \int_{z=-h/2}^{z=h/2} \frac{(-R\sin\beta)}{\left(R^2 + r^2 - 2Rr\cos\beta + (z_K - z)^2\right)^{\frac{3}{2}}} \sin(\alpha
$$
$$
+ \beta) \, dz \, d\beta \quad (A.5)
$$

Integrating Eq. (A.5) based on z yields:

$$
H_{K(\alpha)}^{(3D)}(r, \alpha, z_K) = \frac{JR}{4\pi\mu_0} \int_{\beta=-\pi}^{\beta=\pi} \left. \frac{(z - z_K)(-R\sin\beta)}{\left|\overrightarrow{P'K}\right|^2 \sqrt{\left|\overrightarrow{P'K}\right|^2 + (z_K - z)^2}} \right|_{z=-\frac{h}{2}}^{z=\frac{h}{2}} \sin(\alpha + \beta) d\beta \quad (A.6)
$$

94

Here, $\left|\overrightarrow{P'K}\right|^2$ is calculated using (A.2.1); expanding (A.6) produces:

$$H_{K(\alpha)}^{(3D)}(r, \alpha, z_K)$$

$$= \frac{JR}{4\pi\mu_0} \int_{\beta=-\pi}^{\beta=\pi} \left(\frac{\left(\frac{h}{2} - z_K\right)}{\left|\overrightarrow{P'K}\right|^2 \sqrt{\left|\overrightarrow{P'K}\right|^2 + \left(\frac{h}{2} - z_K\right)^2}} + \frac{\left(\frac{h}{2} + z_K\right)}{\left|\overrightarrow{P'K}\right|^2 \sqrt{\left|\overrightarrow{P'K}\right|^2 + \left(\frac{h}{2} + z_K\right)^2}} \right) (-R\sin\beta)\sin(\alpha$$

$$+ \beta)d\beta$$

or,

$$H_{K(\alpha)}^{(3D)}(r, \alpha, z_K) = \left(\frac{JR}{4\pi\mu_0} \int_{\beta=-\pi}^{\beta=\pi} G\left(\left|\overrightarrow{P'K}\right|^2\right) (-R\sin(\beta))(\cos(\beta)\sin(\alpha) \right.$$

$$\left. + \sin(\beta)\cos(\alpha))d\beta \right) \quad \text{(A.7)}$$

Here,

$$G\left(\left|\overrightarrow{P'K}\right|^2\right) = \frac{\left(\frac{h}{2} - z_K\right)}{\left|\overrightarrow{P'K}\right|^2 \sqrt{\left|\overrightarrow{P'K}\right|^2 + \left(\frac{h}{2} - z_K\right)^2}} + \frac{\left(\frac{h}{2} + z_K\right)}{\left|\overrightarrow{P'K}\right|^2 \sqrt{\left|\overrightarrow{P'K}\right|^2 + \left(\frac{h}{2} + z_K\right)^2}} \quad \text{(A.7.1)}$$

with consideration of periodic odd/even functions in the interval $[-\pi; \pi]$ in equation (A.7), the tangential component is finally expressed as follows:

$$H_{K(\alpha)}^{(3D)}(r, \alpha, z_K) = \left(\frac{JR}{4\pi\mu_0} \int_{\beta=-\pi}^{\beta=\pi} G\left(\left|\overrightarrow{P'K}\right|^2\right) \left(-R\sin^2(\beta)\right) d\beta \right) \cos(\alpha) \quad \text{(A.8)}$$

For point K belonging to the symmetrical plane of the cylinder $z_K = 0$, expression (A.8) can be simplified to

$$H_{K(\alpha)}^{(\text{Fontana})} (r, \alpha, z_K = 0) = \left(\frac{JhR}{4\pi\mu_0} \int_{\beta=-\pi}^{\beta=\pi} \frac{- R\sin^2(\beta)}{|\overrightarrow{P'K}|^2 \sqrt{\left(\frac{h}{2}\right)^2 + |\overrightarrow{P'K}|^2}} d\beta \right) \cos(\alpha)$$

which is presented in the study by Fontana et al. [19].

A.3 The radial component $H_{K(r)}^{(3D)}(r, \alpha, z_K)$

From Eq. (4.2), $H_{K(r)}^{(3D)}(r, \alpha, z_K)$ can be expressed as follows:

$$H_{K(r)}^{(3D)} (r, \alpha, z_K) = \frac{JR}{4\pi\mu_0} \int_{\beta=-\pi}^{\beta=\pi} \int_{z=-h/2}^{z=h/2} \frac{(r - R\cos\beta)}{(R^2+r^2 - 2Rr\cos\beta + (z_K - z)^2)^{\frac{3}{2}}} \sin(\alpha + \beta) \ dz \ d\beta \quad (A.9)$$

Following the same derivation steps as for the tangential component while integrating (A.9) yields:

$$H_{K(r)}^{(3D)}(r, \alpha, z_K) = \left(\frac{JR}{4\pi\mu_0} \int_{\beta=-\pi}^{\beta=\pi} G\left(|\overrightarrow{P'K}|^2\right) (r - R\cos(\beta))(\cos(\beta)\sin(\alpha) + \sin(\beta)\cos(\alpha)) d\beta \right) \quad (A.10)$$

Here, $G\left(|\overrightarrow{P'K}|^2\right)$ is calculated using (A.7.1)

with consideration of periodic odd/even functions in the interval $[-\pi; \pi]$ in Eq. (A.10), the radial component is finally expressed as follows:

$$H_{K(r)}^{(3D)} (r, \alpha, z_K) = \left(\frac{JR}{4\pi\mu_0} \int_{\beta=-\pi}^{\beta=\pi} G\left(\left| \overrightarrow{P'K} \right|^2 \right) (r\cos(\beta) - R\cos^2(\beta)) \, d\beta \right) \sin(\alpha) \quad (A.11)$$

Inserting r = R in equations (A.7.1) and (A.11), Eq. (A.11) is simplified to

$$H_{K(r)}^{(3D)} (r = R, \alpha,$$

$$z_K) = \left(\frac{J}{8\pi\mu_0} \int_{\beta=-\pi}^{\beta=\pi} \left(\frac{\left(\frac{h}{2} - z_K \right)}{\sqrt{\left(\frac{h}{2} - z_K \right)^2 + \left| \overrightarrow{P'K} \right|^2}} + \frac{\left(\frac{h}{2} + z_K \right)}{\sqrt{\left(\frac{h}{2} + z_K \right)^2 + \left| \overrightarrow{P'K} \right|^2}} \right) \cos(\beta) \, d\beta \right) \sin(\alpha)$$

For point K belonging to the symmetrical plane of the cylinder $z_K = 0$, expression (A.11) can be simplified to

$$H_{K(r)}^{(Fontana)} (r, \alpha, z_K = 0) = \left(\frac{JhR}{4\pi\mu_0} \int_{\beta=-\pi}^{\beta=\pi} \frac{r\cos(\beta) - R\cos^2(\beta)}{\left| \overrightarrow{P'K} \right|^2 \sqrt{\left(\frac{h}{2} \right)^2 + \left| \overrightarrow{P'K} \right|^2}} \, d\beta \right) \sin(\alpha)$$

which is presented in the study by Fontana et al. [19].